

Transient solutions to non-linear acousto-magneto-mechanical coupling for axisymmetric MRI scanner design

S. Bagwell^{†1}, P.D. Ledger^{†1}, A.J. Gil^{†1} and M. Mallett[‡]

[†]Zienkiewicz Centre for Computational Engineering, College of Engineering,
Swansea University Bay Campus, Swansea, SA1 8EN, UK

[‡]Siemens Healthcare Ltd., MR Magnet Technology, Wharf Road, Eynsham, Witney, Oxon, OX29 4BP,
UK

November 17, 2017

Abstract

In this work, we simulate the coupled physics describing a Magnetic Resonance Imaging (MRI) scanner by using a *hp*-finite element discretisation and a Newton-Raphson algorithm. To apply the latter, a linearisation of the non-linear system of equations is necessary and we consider two alternative approaches. In the first, the *non-linear approach*, there is no approximation from a physical standpoint and the linearisation is performed about the current solution, in the second, the *linearised approach*, we realise that the MRI problem can be described by small dynamic fluctuations about a dominant static solution and linearise about the latter. The *linearised approach* permits solutions in the frequency domain and provides a computationally efficient way to solve this challenging problem, as it allows the tangent stiffness matrix to be inverted independently of time or frequency. We focus on transient solutions to the coupled system of equations and address the following two important questions; 1) How good is the agreement between the computationally efficient *linearised approach* compared with the intensive *non-linear approach*? and 2) Over what range of MRI operating conditions can the *linearised approach* be expected to provide acceptable results for MRI scanner design? We include a set of academic and industrially relevant examples to benchmark and illustrate our approach.

keywords: *Multifield systems, Finite element methods, Newton methods, Time integration implicit, Linearisation, Acousto-magneto-mechanical coupling, MRI Scanner*

¹(S. Bagwell, P.D. Ledger, A.J. Gil), Zienkiewicz Centre for Computational Engineering, College of Engineering, Swansea University Bay Campus, Swansea, SA1 8EN, UK. E-mail: (scottgbagwell@gmail.com, p.d.ledger@swansea.ac.uk, a.j.gil@swansea.ac.uk)

1 Introduction

In recent years, Magnetic Resonance Imaging (MRI) scanners, illustrated in Figure 1, have become an indispensable tool for use in medical imaging. Their capability to non intrusively diagnose a range of medical ailments, such as tumours [1], damaged cartilage, fractures [2], internal bleeding and even detection of multiple sclerosis [3] make them a desirable imaging technique for clinical use. The increasing accuracy in MRI has become a topic of particular importance in recent years, due to the need for more accurate diagnosis of medical conditions, such as cancer [4, 5].

MRI scanner resolution is determined by the strength of the static magnetic field, \mathbf{H}^{DC} , produced by the main magnet. The magnitude of magnetic flux density of such fields, $|\mathbf{B}^{DC}|$, is typically in the region of 1.5-3T (approximately 30,000 to 70,000 times the strength of that of the Earth) for clinical operation [6, 7, 8], with some 7T units in use for medical research applications [9, 10]. Recently, the Siemens 7T magnet, the MAGNETOM Terra [11], has also been cleared for clinical use as well as use in research. The magnitude of the magnetic flux density, quoted by manufacturers, is defined as the maximum value of the flux density magnitude on the imaging bore axis ², in the centre where the patient lies, shown in Figure 1. Recent advances in MRI design have resulted in magnets of flux densities of up to 12T coming into production, which will allow for very high resolution images to be obtained, compared with the current systems [12]. These scanners all typically utilise superconducting magnets consisting of wound conducting wires, resembling solenoids, that are supercooled by being immersed in liquid helium (to temperatures of approximately 4°K). Some open C-shaped MRI scanners, which utilise permanent magnets to generate the static field, are still available, but these are less common in current imaging units due to their relatively low flux densities of approximately 0.3T.



Figure 1: Patient on MRI scanner bed with localised torso receiver coils, courtesy of Siemens.

In addition to the static field generated by the main magnet, MRI scanners use pulsed time varying magnetic field gradients, generated through sets of resistive coils, which excite the tissues and generate images of the patient. The gradient in the magnetic flux density of these fields is much smaller than the flux density of the main static field, typically with amplitudes in the region of $30-80 \times 10^{-3} \text{ T/m}$ [6, 7, 8] ³. In the presence of conducting bodies, these time varying fields give rise to eddy currents which exert Lorentz forces in the conductors. These forces generate magnetic stresses in the conducting components, which, in turn, causes them to deform and vibrate. Furthermore, these vibrations generate Lorentz currents, which cause further perturbations in the magnetic field. They also cause the surrounding free space region of air to perturb, generating acoustic pressure waves, resulting in audible noise that can cause discomfort for the patient. These generated pressure waves can also rebound off other conducting components causing

²The imaging bore is located in free space and as such $\mathbf{B}^{DC} = \mu_0 \mathbf{H}^{DC}$, where $\mu_0 = 4\pi \times 10^{-7} \text{ H/m}$ is the permeability of free space.

³The gradient field is typically measured in terms of spatial rate of change in the magnetic flux density along the imaging bore axis, in Teslas per metre (T/m). The magnitude of the magnetic flux density arising from these coils is orders of magnitude smaller than that of the main coils.

further deformations to the conductors and more acoustic waves to form. This, in turn, creates further perturbations of the magnetic field resulting in a fully coupled complex system of non-linear transient PDEs comprising the Maxwell, elasticity and acoustic equations [13].

With increasing interest in the design of more economical (reduced amount of material, decreased power consumption) and more advanced MRI systems (capable of producing stronger magnetic fields) [14], of late, the prediction of the physical behaviours of such scanners has become an important area of research, in particular, the computational modelling of these systems. As such, an emphasis on the reduction of the computational cost of such simulations is of great importance to the medical imaging industry. Many single field attempts to analyse the magnetic field of MRI scanners have been published; finite difference time domain methods for the calculation of eddy currents arising from transient gradient coils in MRI scanners [15, 16, 17], with analysis also of the effects on the human body [18, 19, 20], and methods for 'fast' analysis and design of the MRI coils [21, 22]. A number of works have also been published which focus on the analysis of superconducting solenoids [23] as well as the on full MRI scanners [24, 25] and also consider the structural design of higher field scanners [26]. Acoustic effects in MRI scanners have also been investigated [27], with attempts to design noise reduction systems [28, 29] and even analyse the acoustic effects in the human head [30]. More recently, a few attempts to analyse the magneto-mechanical coupling in MRI systems have been considered; with the modelling of axisymmetric superconducting solenoids in self magnetic fields [31] and efficient low order FE solvers for magneto-mechanical coupling in [32], which utilised calculation of body forces to generate a weakly coupled algorithm. This work was later extended to include acoustic effects in [33].

Our previous work in [34] focuses on the solution of coupled magneto-mechanical behaviour of geometrically idealised MRI scanners, with arbitrarily high order finite elements [35, 36], through a stress tensor approach to avoid direct calculation of the electromagnetic body forces. Given the relatively small scale phenomena that emerge in such magnetic and acoustic applications; such as small skin depths in conducting components (known as skin effect) [37] and high frequency acoustic waves, high order elements are necessary to accurately resolve such effects and ensure accurate solutions, as shown in [13]. Furthermore, by choosing to linearise the transient non-linear system of coupled equations about the static fields, the formulation simplifies greatly resulting in a transient linear system of equations dependent on the transient magnetic field excitation, as shown in [13]. Similar techniques, involving the additive split of a non-linear problem to a series of linear problems, have been successfully applied to the field of computational mechanics such as; analysis of structural membranes [38, 39, 40], high order mesh generation [41] and in biomedical applications [42]. This formulation permits a simple *linearised approach* that can be solved in the frequency domain and, given the relatively small frequency ranges of MRI applications, provides rapid solutions to industrial problems. However, the relative importance of the non-linear terms will depend on the strength of the coupling between the acoustic, mechanical and electromagnetic fields. In the context of MRI scanners, it is thus imperative to answer two important questions: 1) How good is the agreement between the computationally efficient *linearised approach* compared with the intensive treatment of the fully non-linear system, denoted the *non-linear approach*? and 2) Over what range of MRI operating conditions can the *linearised approach* be expected to provide acceptable results for MRI scanner design?

The aim of this paper is to address these two questions. This is achieved through the following novelties: 1) We revisit the linearisation of the non-linear equations presented in [13] and provide an alternative formulation, suitable for transient simulation of the full non-linear problem, using a Newton-Raphson and alpha-type time integration schemes. We refer to this as the *non-linear approach*, 2) We rigorously derive bounds on the relative contributions of the non-linear terms in our *non-linear approach* that are not present in the *linearised approach* formulated in [13], and 3) We undertake a rigorous comparison of the *linearised* and *non-linear approaches* for a set of challenging industrially motivated examples.

In this paper, we begin by presenting the coupled transient transmission problem and its associated initial conditions in Section 2. We then briefly summarise the iterative Newton-Raphson procedure of the linearised system of non-linear equations and present it in the form of a dynamic second order system in Section 3. In Section 4, we derive a set of rigorous bounds on the non-linear terms that are; present in the *non-linear approach* and absent in the *linearised approach*. In doing so, we determine a series of measures

for the non-linearity of the acousto-magneto-mechanical coupling in MRI scanners, allowing us to understand the validity of the *linearised approach*. In Section 5, we briefly recall the spatial discretisation of the system by means of high order hp finite elements. We include the temporal discretisation, where we have implemented a second order generalised α -scheme, to allow for inclusion of numerical dissipation into the model. The system is then solved through an iterative monolithic Newton-Raphson solution procedure, which is summarised in an algorithm. We then conclude with numerical results in Section 6.

2 Coupled system

Previously in [13], we presented the fully coupled system of non-linear equations describing the magnetic, mechanic and acoustic behaviours of an MRI scanner. The work included the transmission conditions present at the interface between the conducting and non-conducting regions, as well as initial and far field conditions of the system. From this coupled transmission problem, a simpler linearised scheme was introduced by a suitable additive split of the exciting current source $\mathbf{J}^s(t)$. In this section, we briefly recall the fully coupled transmission problem derived in our earlier paper and focus on the treatment of the transient non-linear problem as a means of verifying our earlier *linearised approach*.

2.1 Transient non-linear system

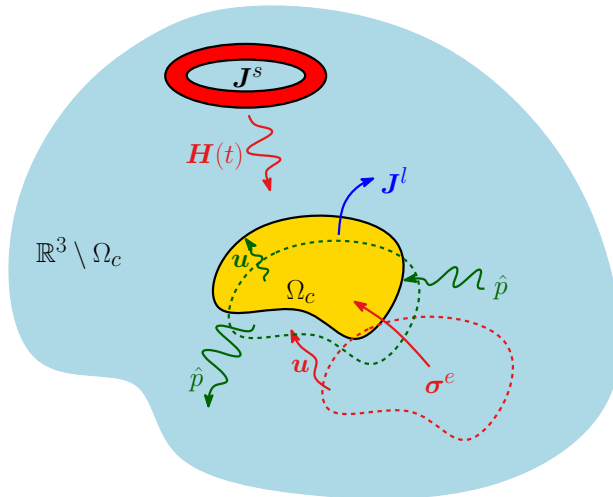


Figure 2: Physical representation of the coupling effects in an MRI environment.

The governing coupled transmission problem, illustrated in Figure 2, describing the acousto-magneto-mechanical behaviour of MRI scanners is given by the following: Find $(\mathbf{A}, \mathbf{u}, \hat{p})(t) \in (\mathbb{R}^3 \times \mathbb{R}^3 \times \mathbb{R})[0, T]$ such that

$$\nabla \times (\mu^{-1} \nabla \times \mathbf{A}) + \gamma \frac{\partial \mathbf{A}}{\partial t} = \mathbf{J}^s + \gamma \frac{\partial \mathbf{u}}{\partial t} \times (\nabla \times \mathbf{A}) \quad \text{in } \mathbb{R}^3, \quad (1a)$$

$$\nabla \cdot \mathbf{A} = 0 \quad \text{in } \mathbb{R}^3 \setminus \Omega_c, \quad (1b)$$

$$\nabla \cdot (\boldsymbol{\sigma}^m(\mathbf{u}) + \boldsymbol{\sigma}^e(\mathbf{A})) = \rho \frac{\partial^2 \mathbf{u}}{\partial t^2} \quad \text{in } \Omega_c, \quad (1c)$$

$$\nabla^2 \hat{p} - \frac{1}{c^2} \frac{\partial^2 \hat{p}}{\partial t^2} = -\nabla \cdot (\nabla \cdot \boldsymbol{\sigma}^e(\mathbf{A})) \quad \text{in } \mathbb{R}^3 \setminus \Omega_c, \quad (1d)$$

$$\mathbf{A} = O(|\mathbf{x}|^{-1}), \quad (1e)$$

$$\lim_{|\mathbf{x}| \rightarrow \infty} \left(\frac{\partial \hat{p}}{\partial |\mathbf{x}|} + \frac{\partial \hat{p}}{\partial t} \right) = O(|\mathbf{x}|^{-1}) \quad \text{as } |\mathbf{x}| \rightarrow \infty, \quad (1f)$$

$$\mathbf{u} = \mathbf{u}^D, \quad (1g)$$

$$\nabla \hat{p}|_{\partial \Omega_c^D}^+ \cdot \mathbf{n} = 0 \quad \text{on } \partial \Omega_c^D, \quad (1h)$$

$$\rho^+ \frac{\partial^2 \mathbf{u}}{\partial t^2} \Big|_{\partial \Omega_c^N}^- \cdot \mathbf{n} = (\nabla \hat{p} + \nabla \cdot \boldsymbol{\sigma}^e(\mathbf{A}))|_{\partial \Omega_c}^+ \cdot \mathbf{n} \quad \text{on } \partial \Omega_c^N, \quad (1i)$$

$$\mathbf{n} \times [\mathbf{A}]_{\partial \Omega_c} = \mathbf{0}, \quad (1j)$$

$$\mathbf{n} \times [\mu^{-1} \nabla \times \mathbf{A}]_{\partial \Omega_c} = \mathbf{0}, \quad (1k)$$

$$(\boldsymbol{\sigma}^e(\mathbf{A}) + \boldsymbol{\sigma}^m(\mathbf{u}))|_{\partial \Omega_c}^- \mathbf{n} = (\hat{p} \mathbf{I} + \boldsymbol{\sigma}^e(\mathbf{A}))|_{\partial \Omega_c}^+ \mathbf{n} \quad \text{on } \partial \Omega_c, \quad (1l)$$

subject to an appropriate set of initial conditions. In (1), the magnetic field \mathbf{H} is defined in terms of the magnetic vector potential \mathbf{A} by $\mathbf{H} = \mu^{-1} \nabla \times \mathbf{A}$, where μ is the magnetic permeability of the medium, \hat{p} is the acoustic pressure field in free space region (of air) $\mathbb{R}^3 \setminus \Omega_c$ and \mathbf{u} is the displacement field of the conducting bodies Ω_c . The eddy currents $\mathbf{J}^e = \gamma \partial \mathbf{A} / \partial t$ and Lorentz currents $\mathbf{J}^l = \gamma \partial \mathbf{u} / \partial t \times (\nabla \times \mathbf{A})$ are expressed in terms of the field variables, respectively. The notation describing the system of equations in (1) is the same as in [13], where; the magnetic vector potential, mechanical displacements and acoustic pressure have been introduced above. \mathbf{J}^s are the magnetic source currents, \mathbf{x} the position vector, γ the electrical conductivity and

$$\boldsymbol{\sigma}^m(\mathbf{u}) := \lambda \text{tr}(\boldsymbol{\varepsilon}(\mathbf{u})) \mathbf{I} + 2G \boldsymbol{\varepsilon}(\mathbf{u}),$$

the Cauchy stress tensor. In the above, λ and G denote the Lamé parameters, ρ the material density, $\boldsymbol{\varepsilon} := (\nabla \mathbf{u} + \nabla \mathbf{u}^T) / 2$ the linear strain tensor, \mathbf{I} the identity tensor, T the transpose, \mathbf{n} the unit normal vector and

$$\boldsymbol{\sigma}^e(\mathbf{A}) := \mu^{-1} \left((\nabla \times \mathbf{A}) \otimes (\nabla \times \mathbf{A}) - \frac{1}{2} |\nabla \times \mathbf{A}|^2 \mathbf{I} \right), \quad (2)$$

the magnetic component of the Maxwell stress tensor.

2.2 Static problem

MRI scanners are driven by time varying current sources through a series of conducting coils and thus the system, in (1), is excited through the current source $\mathbf{J}^s(t)$. During operation, however, MRI scanners typically remain at static field and only apply time varying currents during imaging sequences [43]. This allows for the decomposition of the current source $\mathbf{J}^s(t) = \mathbf{J}^{DC} + \mathbf{J}^{AC}(t)$, where \mathbf{J}^{DC} corresponds to the static current source of the main magnetic coils and $\mathbf{J}^{AC}(t)$ the transient current source of the gradient coils. The solution to the static problem $(\mathbf{A}^{DC}, \mathbf{u}^{DC}, \hat{p}^{DC})$ is achieved by setting $\mathbf{J}^s = \mathbf{J}^{DC}$ and assuming the fields are not time dependent in (1) resulting in the system for $(\mathbf{A}^{DC}, \mathbf{u}^{DC}, \hat{p}^{DC})$, presented in [13, Equation (8)]. After linearising the system and applying a Newton-Raphson scheme the solution to the linear system is obtained by solving [13, Equation (11)].

2.3 Initial conditions

In our previous work, the initial conditions in (1) were set to be zero, such that they represented a system at rest. This corresponds to a MRI scanner with the magnetic field completely switched off. In practice, however, MRI scanners are typically maintained at full field strength, whilst in clinical use, due to the time required for the static magnetic field to reach the desired field strength. The gradient (time varying) fields are then only applied during imaging sequences of the patient. This offers physical motivation to set the initial conditions for (1) to the solution of the static field components and so become

$$\mathbf{A}(t=0) = \mathbf{A}^{DC} \quad \text{in } \mathbb{R}^3, \quad (3a)$$

$$\mathbf{u}(t=0) = \mathbf{u}^{DC}, \quad \frac{\partial \mathbf{u}}{\partial t}(t=0) = \mathbf{0} \quad \text{in } \Omega_c, \quad (3b)$$

$$\hat{p}(t=0) = \hat{p}^{DC}, \quad \frac{\partial \hat{p}}{\partial t}(t=0) = \mathbf{0} \quad \text{in } \mathbb{R}^3 \setminus \Omega_c. \quad (3c)$$

Setting these as initial conditions for the system in (1) allows us to solve the, much larger, static component independent of time and then start the transient simulations from this point. With the knowledge of the

static field, only solutions of the transient components of the fields at each time instance are required, resulting in shorter simulation times. This choice also more accurately represents an MRI scanner during actual clinical use.

3 Linearisation

The transient problem in (1) presents a non-linear system of coupled equations describing electromagnetic, mechanic and acoustic behaviours in an MRI environment. In this section we briefly recall the linearisations of (1) in [13, Equations (12) and (13)] and [13, Equations (14) and (15)] and present our *non-linear* and *linearised approaches*, respectively, for the solution of (1). We then focus on the construction of the linearised dynamic system of equations by separating out the terms involving the first and second temporal derivatives. This representation, after applying spatial discretisation, will allow for the transient system to be presented in terms of a dynamic system involving mass, damping and stiffness matrices.

3.1 Non-linear approach

3.1.1 Coupled weak form

The solution of the linearised system of weak equations for the non-linear transmission problem in (1) is expressed in the form of the following iterative Newton-Raphson procedure: Find $(\delta_A^{[k]}, \delta_u^{[k]}, \delta_{\hat{p}}^{[k]}) \in X \times Y(\mathbf{0}) \times Z$ such that

$$\begin{aligned} DR_A(\mathbf{A}^\delta; \mathbf{A}^{[k]}, \mathbf{u}^{[k]})[\delta_A^{[k]}] + DR_A(\mathbf{A}^\delta; \mathbf{A}^{[k]}, \mathbf{u}^{[k]})[\delta_u^{[k]}] \\ = -R_A(\mathbf{A}^\delta; \mathbf{A}^{[k]}, \mathbf{u}^{[k]}), \end{aligned} \quad (4a)$$

$$\begin{aligned} DR_u(\mathbf{u}^\delta; \mathbf{A}^{[k]}, \mathbf{u}^{[k]}, \hat{p}^{[k]})[\delta_A^{[k]}] + DR_u(\mathbf{u}^\delta; \mathbf{A}^{[k]}, \mathbf{u}^{[k]}, \hat{p}^{[k]})[\delta_u^{[k]}] + DR_u(\mathbf{u}^\delta; \mathbf{A}^{[k]}, \mathbf{u}^{[k]}, \hat{p}^{[k]})[\delta_{\hat{p}}^{[k]}] \\ = -R_u(\mathbf{u}^\delta; \mathbf{A}^{[k]}, \mathbf{u}^{[k]}, \hat{p}^{[k]}), \end{aligned} \quad (4b)$$

$$\begin{aligned} DR_{\hat{p}}(\hat{p}^\delta; \mathbf{A}^{[k]}, \mathbf{u}^{[k]}, \hat{p}^{[k]})[\delta_A^{[k]}] + DR_{\hat{p}}(\hat{p}^\delta; \mathbf{A}^{[k]}, \mathbf{u}^{[k]}, \hat{p}^{[k]})[\delta_u^{[k]}] + DR_{\hat{p}}(\hat{p}^\delta; \mathbf{A}^{[k]}, \mathbf{u}^{[k]}, \hat{p}^{[k]})[\delta_{\hat{p}}^{[k]}] \\ = -R_{\hat{p}}(\hat{p}^\delta; \mathbf{A}^{[k]}, \mathbf{u}^{[k]}, \hat{p}^{[k]}), \end{aligned} \quad (4c)$$

for all $(\mathbf{A}^\delta, \mathbf{u}^\delta, \hat{p}^\delta) \in X \times Y(\mathbf{0}) \times Z$ for a particular iteration $[k]$, where the system of weak variational residuals and their directional derivatives are defined in [13, Equations (12) and (13)] respectively and obtained by adopting the approach in [44]. We introduce the following definitions

$$\begin{aligned} X &:= \{\mathbf{A} \in \mathbf{H}(\text{curl}, \mathbb{R}^3) : \nabla \cdot \mathbf{A} = 0 \text{ in } \mathbb{R}^3 \setminus \Omega_c\}, \\ Y(\mathbf{g}) &:= \{\mathbf{u} \in H^1(\Omega_c)^3 : \mathbf{u} = \mathbf{g} \text{ on } \partial\Omega_c^D\}, \\ Z &:= \{\hat{p} \in H^1(\mathbb{R}^3 \setminus \Omega_c)\}, \end{aligned}$$

to describe the weak solutions to the transmission problem in (1), where $\mathbf{H}(\text{curl}, \mathbb{R}^3)$ and $H^1(\mathbb{R}^3)$ have their usual definitions e.g. [45].

The solution fields are obtained by first defining an initial guess of the three fields $(\mathbf{A}^{[0]}, \mathbf{u}^{[0]}, \hat{p}^{[0]})$ and then solving (4) to obtain the solution updates $(\delta_A^{[k]}, \delta_u^{[k]}, \delta_{\hat{p}}^{[k]})$. The solution fields are then updated, for a given iteration, by summing the solution field of the previous iteration and the solution updates

$$\begin{aligned} \mathbf{A}^{[k+1]} &= \mathbf{A}^{[k]} + \delta_A^{[k]}, \\ \mathbf{u}^{[k+1]} &= \mathbf{u}^{[k]} + \delta_u^{[k]}, \\ \hat{p}^{[k+1]} &= \hat{p}^{[k]} + \delta_{\hat{p}}^{[k]}, \end{aligned}$$

until $|R_A, R_u, R_{\hat{p}}| < \text{TOL}$ where TOL is a user supplied tolerance. The resulting solutions are $\mathbf{A}(t), \mathbf{u}(t)$ and $\hat{p}(t)$. Equation (4) is similar to the static Newton-Raphson system presented in [13, Equation (11)]. However, given that it is a transient system, will require more than a single iteration to converge, due to the non-linearities present in the transient terms. But the residuals $(R_A, R_u, R_{\hat{p}})$ will converge quadratically to 0.

3.1.2 Reformulation of the Newton-Raphson procedure

With a view to introducing an alternative formulation of (4), in which the terms associated with the zeroth-, first- and second- temporal derivative are isolated, we recast the problem in terms of a vector of unknowns containing the three physical fields $\mathbf{q} := \{\mathbf{q}_A \ \mathbf{q}_u \ q_{\hat{p}}\}^T = \{\mathbf{A} \ \mathbf{u} \ \hat{p}\}^T$. The discretised bilinear forms associated with these temporal derivatives will later form the mass, damping and stiffness terms in our fully discrete approach. This separation allows us to recast Equation (4) and introduce the Newton-Raphson iteration: Find $\delta_q^{[k]} \in W$ at each time $t \in (0, T]$, such that

$$M \left(\frac{\partial^2 \delta_q}{\partial t^2}^{[k]}, \mathbf{q}^\delta \right) + C \left(\frac{\partial \delta_q}{\partial t}^{[k]}, \mathbf{q}^\delta; \mathbf{q}^{[k]} \right) + K \left(\delta_q^{[k]}, \mathbf{q}^\delta; \mathbf{q}^{[k]}, \frac{\partial \mathbf{q}}{\partial t}^{[k]} \right) = -R_q \left(\mathbf{q}^\delta; \mathbf{q}^{[k]}, \frac{\partial \mathbf{q}}{\partial t}^{[k]}, \frac{\partial^2 \mathbf{q}}{\partial t^2}^{[k]} \right), \quad (5)$$

for all $\mathbf{q}^\delta \in W$, where the updated solution vector is

$$\mathbf{q}^{[k+1]} = \mathbf{q}^{[k]} + \delta_q^{[k]}, \quad (6)$$

and $W := X \times Y(\mathbf{0}) \times Z$. The system is iterated until $|R_q| < \text{TOL}$ and the resulting solution is $\mathbf{q}(t)$. The forms of M , C and K , which are associated with the mass, damping and stiffness contributions to the system, respectively, arise from this splitting of the directional derivatives and are given as

$$M \left(\frac{\partial^2 \delta_q}{\partial t^2}^{[k]}, \mathbf{q}^\delta \right) := \int_{\Omega_c} \rho \frac{\partial^2 \delta_u}{\partial t^2}^{[k]} \cdot \mathbf{q}_u^\delta d\Omega - \int_{\partial \Omega_c^N} \rho^+ \frac{\partial^2 \delta_u}{\partial t^2}^{[k]} \Big|^- \cdot \mathbf{n}^+ q_{\hat{p}}^\delta ds \\ + \int_{\mathbb{R}^3 \setminus \Omega_c} \frac{1}{c^2} \frac{\partial^2 \delta_{\hat{p}}}{\partial t^2}^{[k]} \cdot q_{\hat{p}}^\delta d\Omega, \quad (7a)$$

$$C \left(\frac{\partial \delta_q}{\partial t}^{[k]}, \mathbf{q}^\delta; \mathbf{q}^{[k]} \right) := \int_{\mathbb{R}^3} \gamma \frac{\partial \delta_A}{\partial t}^{[k]} \cdot \mathbf{q}_A^\delta d\Omega - \int_{\Omega_c} \gamma \frac{\partial \delta_u}{\partial t}^{[k]} \times (\nabla \times \mathbf{q}_A^{[k]}) \cdot \mathbf{q}_A^\delta d\Omega, \quad (7b)$$

$$K \left(\delta_q^{[k]}, \mathbf{q}^\delta; \mathbf{q}^{[k]}, \frac{\partial \mathbf{q}}{\partial t}^{[k]} \right) := \int_{\mathbb{R}^3} \mu^{-1} (\nabla \times \delta_A^{[k]}) \cdot (\nabla \times \mathbf{q}_A^\delta) d\Omega - \int_{\Omega_c} \gamma \frac{\partial \mathbf{q}_u}{\partial t}^{[k]} \times (\nabla \times \delta_A^{[k]}) \cdot \mathbf{q}_A^\delta d\Omega \\ + \int_{\Omega_c} \mu^{-1} \mathcal{S}(\mathbf{q}_A^{[k]}, \delta_A^{[k]}) : \nabla \mathbf{q}_u^\delta d\Omega - \int_{\partial \Omega_c^N} \mu_0^{-1} \mathcal{S}(\mathbf{q}_A^{[k]}, \delta_A^{[k]}) |^+ \mathbf{n}^- \cdot \mathbf{q}_u^\delta ds \\ + \int_{\Omega_c} \boldsymbol{\sigma}^m(\delta_u^{[k]}) : \nabla \mathbf{q}_u^\delta d\Omega - \int_{\partial \Omega_c^N} \delta_{\hat{p}}^{[k]} |^+ \mathbf{n}^- \cdot \mathbf{q}_u^\delta ds \\ - \int_{\text{supp}(\mathbf{J}^s)} \left(\nabla \times \delta_A^{[k]} \times (\nabla \times (\mu_0^{-1} \nabla \times \mathbf{q}_A^{[k]})) \right. \\ \left. + \nabla \times \mathbf{q}_A^{[k]} \times (\nabla \times (\mu_0^{-1} \nabla \times \delta_A^{[k]})) \right) \cdot \nabla q_{\hat{p}}^\delta d\Omega \\ + \int_{\mathbb{R}^3 \setminus \Omega_c} \nabla \delta_{\hat{p}}^{[k]} \cdot \nabla q_{\hat{p}}^\delta d\Omega, \quad (7c)$$

where the corresponding matrices will follow from their discrete counterparts, which we will discuss in Section 5. The system residual vector R_q is defined as

$$R_q \left(\mathbf{q}^\delta; \mathbf{q}^{[k]}, \frac{\partial \mathbf{q}}{\partial t}^{[k]}, \frac{\partial^2 \mathbf{q}}{\partial t^2}^{[k]} \right) := M \left(\frac{\partial^2 \mathbf{q}}{\partial t^2}^{[k]}, \mathbf{q}^\delta \right) + C \left(\frac{\partial \mathbf{q}}{\partial t}^{[k]}, \mathbf{q}^\delta; \mathbf{q}^{[k]} \right) \\ + \int_{\mathbb{R}^3} \mu^{-1} (\nabla \times \mathbf{q}_A^{[k]}) \cdot (\nabla \times \mathbf{q}_A^\delta) d\Omega + \int_{\Omega_c} (\boldsymbol{\sigma}^m(\mathbf{q}_u^{[k]}) + \boldsymbol{\sigma}^e(\mathbf{q}_A^{[k]})) : \nabla \mathbf{q}_u^\delta d\Omega \\ - \int_{\partial \Omega_c^N} (q_{\hat{p}}^{[k]} \mathbf{I} + \boldsymbol{\sigma}^e(\mathbf{q}_A^{[k]})) |^+ \mathbf{n}^- \cdot \mathbf{q}_u^\delta ds + \int_{\mathbb{R}^3 \setminus \Omega_c} \left(\nabla q_{\hat{p}}^{[k]} \cdot \nabla q_{\hat{p}}^\delta + (\nabla \cdot \boldsymbol{\sigma}^e(\mathbf{q}_A^{[k]})) \cdot \nabla q_{\hat{p}}^\delta \right) d\Omega$$

$$-\int_{\mathbb{R}^3} \mathbf{J}^s(t) \cdot \mathbf{q}_A^\delta d\Omega. \quad (8)$$

The linearised electromagnetic stress tensor, introduced previously in [13], is expressed in terms of the magnetic vector potential $\mathbf{q}_A = \mathbf{A}$ and its update δ_A as

$$\mathcal{S}(\mathbf{q}_A^{[k]}, \delta_A^{[k]}) := (\nabla \times \mathbf{q}_A)^{[k]} \otimes (\nabla \times \delta_A)^{[k]} + (\nabla \times \delta_A)^{[k]} \otimes (\nabla \times \mathbf{q}_A)^{[k]} - \left((\nabla \times \mathbf{q}_A^{[k]}) \cdot (\nabla \times \delta_A^{[k]}) \right) \mathbf{I}.$$

The initial guesses of the system in (5) and (6) are such that $(\mathbf{q}^{[0]}, \frac{\partial \mathbf{q}}{\partial t}^{[0]}, \frac{\partial^2 \mathbf{q}}{\partial t^2}^{[0]}) \in (X \times Y(\mathbf{u}^D) \times Z) \times (X \times Y(\partial \mathbf{u}^D / \partial t) \times Z) \times (X \times Y(\partial^2 \mathbf{u}^D / \partial t^2) \times Z)$.

3.2 Linearised approach

For completeness, we also state the transient version of the *linearised approach* derived in [13, Equations (14) and (15)]. We set $\mathbf{q}^{DC} := \{\mathbf{A}^{DC}, \mathbf{u}^{DC}, \hat{p}^{DC}\}^T$ as the static solution, which can be obtained from solving [13, Equation (11)] or similarly from (5) by looking for a time invariant solution and replacing \mathbf{J}^{AC} with \mathbf{J}^{DC} . Then, in light of the fact that the linearisation of the coupled non-linear system about \mathbf{q}^{DC} results in a system that is linear in the solution variables, we can recast it in a similar manner to (4), where the system is independent of iterations, as: Find $\delta_q \in W$, such that

$$\tilde{M} \left(\frac{\partial^2 \mathbf{q}}{\partial t^2}, \mathbf{q}^\delta \right) + \tilde{C} \left(\frac{\partial \mathbf{q}}{\partial t}, \mathbf{q}^\delta \right) + \tilde{K} \left(\mathbf{q}, \mathbf{q}^\delta \right) = -\tilde{R}_q \left(\mathbf{q}^\delta \right), \quad (9)$$

for all $\mathbf{q}^\delta \in W$ at each time $t \in [0, T]$. The bilinear forms \tilde{M} , \tilde{C} and \tilde{K} will, once discretised, form the separated mass, damping and stiffness matrices in the *linearised approach*, and can be expressed in terms of the definitions in (7) as

$$\tilde{M} \left(\frac{\partial^2 \delta_q}{\partial t^2}, \mathbf{q}^\delta \right) := M \left(\frac{\partial^2 \delta_q}{\partial t^2}, \mathbf{q}^\delta \right), \quad (10a)$$

$$\tilde{C} \left(\frac{\partial \delta_q}{\partial t}, \mathbf{q}^\delta \right) := C \left(\frac{\partial \delta_q}{\partial t}, \mathbf{q}^\delta; \mathbf{q}^{DC} \right), \quad (10b)$$

$$\tilde{K} \left(\delta_q, \mathbf{q}^\delta \right) := K \left(\delta_q, \mathbf{q}^\delta; \mathbf{q}^{DC}, \mathbf{0} \right), \quad (10c)$$

$$\tilde{R}_q \left(\mathbf{q}^\delta \right) := R_q \left(\mathbf{q}^\delta; \mathbf{q}^{DC}, \mathbf{0}, \mathbf{0} \right). \quad (10d)$$

The system in (9) is independent of iterations and so can be solved in a single step, hence named the *linearised approach*. In this case the solution we obtain from (9) is $\delta_q(t)$, which contains only the transient component of the fields, and thus the complete fields are described as $\mathbf{q}(t) = \mathbf{q}^{DC} + \delta_q(t)$, where \mathbf{q}^{DC} is given from the initial conditions. The linear nature of this system also allows for a time harmonic description of the transient components of the fields to be adopted, which was the approach followed in [13].

4 Non-linear vs. linearised approaches

The *linearised approach*, described in Section 3.2, provides an efficient way of solving the fully coupled acousto-magneto-mechanical problem as the discretisation of (9) results in system matrices that are independent of time, or frequency (if a time harmonic description is used). In particular, by performing the linearisation about the static solution, the non-linear terms in (5) disappear. The relative importance of these terms will depend on a comparison between the magnitudes of the terms in the two *approaches* for the transient and static fields. In this section, we first analyse and compare the magnitudes of the non-linear terms present in the *non-linear approach* with the terms in the *linearised approach*. We then summarise the measures of interest, derived in this comparison, that determine the non-linearity of the problem. Finally, we summarise a simple analytical model that can relate these measures to manufacturing data in order to analyse the operating range of magnetic field strengths used in actual MRI scanners.

4.1 Comparison of linearised and non-linear terms

In order to determine if the *linearised approach*, presented in Section 3.2, accurately approximates the solution to the *non-linear approach* (4), at a continuous level, we must compare the magnitude of the non-linear terms arising in the *non-linear approach* with the corresponding terms in the *linearised approach*. By comparison of the two approaches, four terms in the linearisation differ between the *non-linear* and *linearised approaches*. These differences, composing of three stiffness contribution terms and a damping contribution term, are; $DR_A[\delta_A]$, $DR_A[\delta_u]$, $DR_u[\delta_A]$ and $DR_p[\delta_A]$, presented in [13, Equations (13a), (13b), (13c) and (13f), respectively].

4.1.1 $DR_A[\delta_A]$ term

The first term which differs between the two approaches is the directional derivative of the Lorentz currents with respect to the magnetic vector potential $DR_A[\delta_A]$ in [13, (13a)]. If we first take the magnitude of this term and apply the Cauchy-Schwartz inequality, we obtain the following bound

$$\begin{aligned} I_1(t) := \left| \int_{\Omega_c} \gamma \frac{\partial \mathbf{u}}{\partial t} \times (\nabla \times \boldsymbol{\delta}_A) \cdot \mathbf{A}^\delta d\Omega \right| &\leq \left(\int_{\Omega_c} |\mathbf{A}^\delta|^2 d\Omega \right)^{\frac{1}{2}} \left(\int_{\Omega_c} \left| \gamma \frac{\partial \mathbf{u}}{\partial t} \right|^2 d\Omega \right)^{\frac{1}{2}} \left(\int_{\Omega_c} |\nabla \times \boldsymbol{\delta}_A|^2 d\Omega \right)^{\frac{1}{2}} \\ &\leq \left\| \mathbf{A}^\delta \right\|_{L^2(\Omega_c)} \left\| \gamma \frac{\partial \mathbf{u}}{\partial t} \right\|_{L^2(\Omega_c)} \|\nabla \times \boldsymbol{\delta}_A\|_{L^2(\Omega_c)} \\ &\leq C_1 \left\| \gamma \frac{\partial \mathbf{u}^{AC}}{\partial t} \right\|_{L^\infty(\Omega_c)} \|\boldsymbol{\delta}_B\|_{L^\infty(\Omega_c)}, \end{aligned} \quad (11)$$

where we have used $\mathbf{u} = \mathbf{u}^{DC} + \mathbf{u}^{AC}$ and $\boldsymbol{\delta}_B = \nabla \times \boldsymbol{\delta}_A$ and note that $\partial \mathbf{u}^{DC} / \partial t = \mathbf{0}$. We also use the fact that the L^2 norm is bounded by $\|\cdot\|_{L^2(\Omega_c)} \leq D \|\cdot\|_{L^\infty(\Omega_c)}$ and D is a constant that depends on the size of the domain Ω_c . We include $\|\mathbf{A}^\delta\|_{L^2(\Omega_c)}$, which for the numerical experiments presented later in this work will be chosen to be bounded finite element basis functions, in the constant C_1 , which is independent of field strength and material parameters.

4.1.2 $DR_A[\delta_u]$ term

The second term in the *non-linear approach*, which differs from that of the *linearised approach*, is the directional derivative of the Lorentz currents with respect to the displacement field $DR_A[\delta_u]$ in [13, Equation (13b)]. Again, taking the magnitude of this term and applying the Cauchy-Schwartz inequality we obtain the following bound

$$\begin{aligned} I_2(t) := \left| \int_{\Omega_c} \gamma \left(\frac{\partial \boldsymbol{\delta}_u}{\partial t} \times (\nabla \times \mathbf{A}) \right) \cdot \mathbf{A}^\delta d\Omega \right| &\leq \left(\int_{\Omega_c} |\mathbf{A}^\delta|^2 d\Omega \right)^{\frac{1}{2}} \left(\int_{\Omega_c} \left| \gamma \frac{\partial \boldsymbol{\delta}_u}{\partial t} \right|^2 d\Omega \right)^{\frac{1}{2}} \left(\int_{\Omega_c} |\nabla \times \mathbf{A}|^2 d\Omega \right)^{\frac{1}{2}} \\ &\leq C_2 \left\| \gamma \frac{\partial \boldsymbol{\delta}_u}{\partial t} \right\|_{L^\infty(\Omega_c)} \|\mathbf{B}^{DC} + \mathbf{B}^{AC}\|_{L^\infty(\Omega_c)}, \end{aligned} \quad (12)$$

where we have applied the same steps as in (11) and split the magnetic flux density field as $\mathbf{B} = \mathbf{B}^{DC} + \mathbf{B}^{AC}$. The corresponding term from the linear system in [13, Equation (15b)], where the fields are linearised about the static solution, is given by

$$I_2^{lin}(t) \leq C_2^{lin} \left\| \gamma \frac{\partial \boldsymbol{\delta}_u}{\partial t} \right\|_{L^\infty(\Omega_c)} \|\mathbf{B}^{DC}\|_{L^\infty(\Omega_c)}. \quad (13)$$

The extent of non-linearity of the non-linear problem is determined by the magnitude of this term compared with its counterpart in the *linearised approach*. The ratio of the magnitudes of the two terms is bounded by

$$\frac{I_2(t)}{I_2^{lin}(t)} \leq C \frac{\|\mathbf{B}^{DC} + \mathbf{B}^{AC}\|_{L^\infty(\Omega_c)}}{\|\mathbf{B}^{DC}\|_{L^\infty(\Omega_c)}}$$

$$\begin{aligned}
&\leq C \frac{\|\mathbf{B}^{DC}\|_{L^\infty(\Omega_c)} + \|\mathbf{B}^{AC}\|_{L^\infty(\Omega_c)}}{\|\mathbf{B}^{DC}\|_{L^\infty(\Omega_c)}} \\
&\leq C \left(1 + \frac{\|\mathbf{B}^{AC}\|_{L^\infty(\Omega_c)}}{\|\mathbf{B}^{DC}\|_{L^\infty(\Omega_c)}} \right), \tag{14}
\end{aligned}$$

where the constant $C = C_2/C_2^{lin}$ depends on the ratio of $\|\gamma \frac{\partial \boldsymbol{\delta}_u}{\partial t}\|_{L^\infty(\Omega_c)}$ evaluated for the *linearised* and *non-linear approaches*, which we assume to be bounded.

4.1.3 $DR_u[\boldsymbol{\delta}_A]$ term

The third term in the *non-linear approach*, which differs from that of the *linearised approach*, is the directional derivative of the Maxwell stress with respect to the magnetic vector potential $DR_u[\boldsymbol{\delta}_A]$ in [13, Equation (13c)]. If we take, first, the magnitude of the volumetric part of this term and apply the Cauchy-Schwartz inequality we obtain the following bound

$$\begin{aligned}
I_3(t) := \left| \int_{\Omega_c} \mu^{-1} \mathcal{S}(\mathbf{A}, \boldsymbol{\delta}_A) : \nabla \mathbf{u}^\delta d\Omega \right| &\leq \left(\int_{\Omega_c} |\nabla \mathbf{u}^\delta|^2 d\Omega \right)^{\frac{1}{2}} \left(\int_{\Omega_c} |\mu^{-1} \mathcal{S}(\mathbf{A}, \boldsymbol{\delta}_A)|^2 d\Omega \right)^{\frac{1}{2}} \\
&\leq C_3 \|\mu^{-1} \mathcal{S}(\mathbf{A}, \boldsymbol{\delta}_A)\|_{L^\infty(\Omega_c)} \\
&\leq C_3 \|\mu^{-1} (\mathbf{B} \otimes \boldsymbol{\delta}_B + \boldsymbol{\delta}_B \otimes \mathbf{B} - (\mathbf{B} \cdot \boldsymbol{\delta}_B) \mathbf{I})\|_{L^\infty(\Omega_c)} \\
&\leq C_3 \max(\mu_{\Omega_c}^{-1}) \|\mathbf{B}^{DC} + \mathbf{B}^{AC}\|_{L^\infty(\Omega_c)} \|\boldsymbol{\delta}_B\|_{L^\infty(\Omega_c)}, \tag{15}
\end{aligned}$$

where μ_{Ω_c} defines the permeability of the conducting medium Ω_c . In (15), we have followed similar steps to Section 4.1.1 in deriving the magnitude of this non-linear term. The magnitude of the corresponding term from the *linearised approach* in [13, Equation (15c)], where the fields are linearised about the static solution, is given by

$$I_3^{lin}(t) \leq C_3^{lin} \max(\mu_{\Omega_c}^{-1}) \|\mathbf{B}^{DC}\|_{L^\infty(\Omega_c)} \|\boldsymbol{\delta}_B\|_{L^\infty(\Omega_c)}. \tag{16}$$

The ratio between the magnitudes of the two terms is bounded by

$$\frac{I_3(t)}{I_3^{lin}(t)} \leq C \left(1 + \frac{\|\mathbf{B}^{AC}\|_{L^\infty(\Omega_c)}}{\|\mathbf{B}^{DC}\|_{L^\infty(\Omega_c)}} \right), \tag{17}$$

where we have applied the same logic as in (14) and the constant $C = C_3/C_3^{lin}$ depends on the ratio of $\|\boldsymbol{\delta}_B\|_{L^\infty(\Omega_c)}$ evaluated for the *linearised* and *non-linear approaches*, which we assume to be bounded.

A similar analysis for the linearisation of the boundary component of the Maxwell stress with respect to the magnetic vector potential in [13, Equation (13c)] provides the same result as (17) but limited to the boundary of the conducting region $\partial\Omega_c$.

4.1.4 $DR_p[\boldsymbol{\delta}_A]$ term

The final term which differs from that of the *linearised approach* is the directional derivative of the Maxwell stress divergence term in the coils with respect to the magnetic vector potential $DR_p[\boldsymbol{\delta}_A]$ in [13, Equation (13f)]. If we take, first, the magnitude of the first part of the term and apply the Cauchy-Schwartz inequality we obtain the following bound

$$\begin{aligned}
I_4(t) := \left| \int_{\text{supp}(\mathbf{J}^s)} ((\nabla \times \boldsymbol{\delta}_A) \times \mathbf{J}^s) \cdot \nabla \hat{p}^\delta d\Omega \right| &\leq \left(\int_{\text{supp}(\mathbf{J}^s)} |\nabla \hat{p}^\delta|^2 d\Omega \right)^{\frac{1}{2}} \left(\int_{\text{supp}(\mathbf{J}^s)} |\nabla \times \boldsymbol{\delta}_A \times \mathbf{J}^s|^2 d\Omega \right)^{\frac{1}{2}} \\
&\leq C_4 \|\boldsymbol{\delta}_B\|_{L^\infty(\text{supp}(\mathbf{J}^s))} \|\mathbf{J}^{DC} + \mathbf{J}^{AC}\|_{L^\infty(\text{supp}(\mathbf{J}^s))}, \tag{18}
\end{aligned}$$

where we have followed similar steps to Section 4.1.1 in deriving the magnitude of this non-linear term and split the current source into $\mathbf{J}^s = \mathbf{J}^{DC} + \mathbf{J}^{AC}$. The magnitude of the corresponding term from the *linearised approach*, in [13, Equation (15f)], is given by

$$I_4^{lin}(t) \leq C_4^{lin} \|\boldsymbol{\delta}_B\|_{L^\infty(\text{supp}(\mathbf{J}^s))} \|\mathbf{J}^{DC}\|_{L^\infty(\text{supp}(\mathbf{J}^s))}. \quad (19)$$

The extent of non-linearity of the non-linear problem is determined by the magnitude of this term compared to its counterpart in the *linearised approach*. The ratio of the magnitudes of the two terms is bounded by

$$\frac{I_4(t)}{I_4^{lin}(t)} \leq C \left(1 + \frac{\|\mathbf{J}^{AC}\|_{L^\infty(\text{supp}(\mathbf{J}^s))}}{\|\mathbf{J}^{DC}\|_{L^\infty(\text{supp}(\mathbf{J}^s))}} \right), \quad (20)$$

where the constant $C = C_4/C_4^{lin}$ is a function only of the ratio of $\|\boldsymbol{\delta}_B\|_{L^\infty(\text{supp}(\mathbf{J}^s))}$ evaluated for the *linearised* and *non-linear approaches*, which we assume to be bounded. Practically speaking, this means that the *linearised approach* will induce a negligible error, in neglecting the term $DR_{\hat{p}}[\boldsymbol{\delta}_A]$, provided that the magnitude of the AC current source is orders of magnitude less than that of the DC current source, which is the case for MRI scanners.

If we now apply the same analysis to the second term in [13, Equation (13f)] we obtain the bound

$$I_5(t) \leq C_5 \|\mathbf{B}^{DC} + \mathbf{B}^{AC}\|_{L^\infty(\text{supp}(\mathbf{J}^s))} \|\nabla \times \boldsymbol{\delta}_B\|_{L^\infty(\text{supp}(\mathbf{J}^s))}, \quad (21)$$

where the material permeability is contained within the constant C_5 , and to the second term in the linear system in [13, Equation (13f)] gives

$$I_5^{lin}(t) \leq C_5^{lin} \|\mathbf{B}^{DC}\|_{L^\infty(\text{supp}(\mathbf{J}^s))} \|\nabla \times \boldsymbol{\delta}_B\|_{L^\infty(\text{supp}(\mathbf{J}^s))}. \quad (22)$$

Again, the ratio of the magnitudes of the two terms is bounded by

$$\frac{I_5(t)}{I_5^{lin}(t)} \leq C \left(1 + \frac{\|\mathbf{B}^{AC}\|_{L^\infty(\text{supp}(\mathbf{J}^s))}}{\|\mathbf{B}^{DC}\|_{L^\infty(\text{supp}(\mathbf{J}^s))}} \right), \quad (23)$$

where the constant $C = C_5/C_5^{lin}$ is a function only of the ratio of $\|\nabla \times \boldsymbol{\delta}_B\|_{L^\infty(\text{supp}(\mathbf{J}^s))}$ evaluated for the *linearised* and *non-linear approaches*, which we assume to be bounded.

4.2 Ratio of the magnetic field strengths

In summary, we see that the *linearised approach* is expected to offer good agreement with the *non-linear approach* provided that the following criteria are met:

- 1) $\|\gamma \partial \mathbf{u}^{AC} / \partial t\|_{L^\infty(\Omega_c)} \|\boldsymbol{\delta}_B\|_{L^\infty(\Omega_c)} \ll 1$,
- 2) $\|\mathbf{B}^{AC}\|_{L^\infty(\Omega)} / \|\mathbf{B}^{DC}\|_{L^\infty(\Omega)} \ll 1$,
- 3) $\|\mathbf{J}^{AC}\|_{L^\infty(\text{supp}(\mathbf{J}^s))} / \|\mathbf{J}^{DC}\|_{L^\infty(\text{supp}(\mathbf{J}^s))} \ll 1$,

where 2) has been generalised to the whole domain Ω , combining the coils, conductors and free space regions.

In the case of 1) the update $\|\boldsymbol{\delta}_B\|_{L^\infty(\Omega_c)}$ at any time instant t will be small, but the conductivity of the material is high. Thus, small velocities are needed for the *linearised approach* to be applicable. For 2) The \mathbf{B}^{DC} field is driven by the strong main magnet and consequently $\|\mathbf{B}^{DC}\|_{L^\infty(\Omega)}$ is orders of magnitude larger than $\|\mathbf{B}^{AC}\|_{L^\infty(\Omega)}$, which results from the AC coils and field perturbations caused by eddy and Lorentz currents in the conductors. For 3) MRI coils are designed such that the current strengths are fairly uniform over the main magnet and gradient coils [46]. Thus $\|\mathbf{J}^{DC}\|_{L^\infty(\text{supp}(\mathbf{J}^s))} = |\mathbf{J}^{DC}|$, $\|\mathbf{J}^{AC}\|_{L^\infty(\text{supp}(\mathbf{J}^s))} = |\mathbf{J}^{AC}|$ and, in current MRI applications $|\mathbf{J}^{AC}| < |\mathbf{J}^{DC}|$. Thus, provided the velocities of the conductors are small the *linearised approach* is expected to give good agreement with the *non-linear approach*.

4.3 Simple model relating field and current strengths

Whilst the true field strength $\mathbf{B} = \mu\mathbf{H}$ can only be found after solving (1) by means of the *non-linear* or *linearised approaches*, described in Section 3, there is merit in also considering a simple model to relate \mathbf{B} to the applied current density in the coils. This is because manufacturer's data, available for MRI scanners, is typically only quoted in terms of the maximum capable main and gradient field strengths at the central axis of the imaging bore [6, 7, 8]. Therefore, in order to determine the operating ranges of the current densities on in-use scanners, the relationships given by this simplified model offer useful insight.

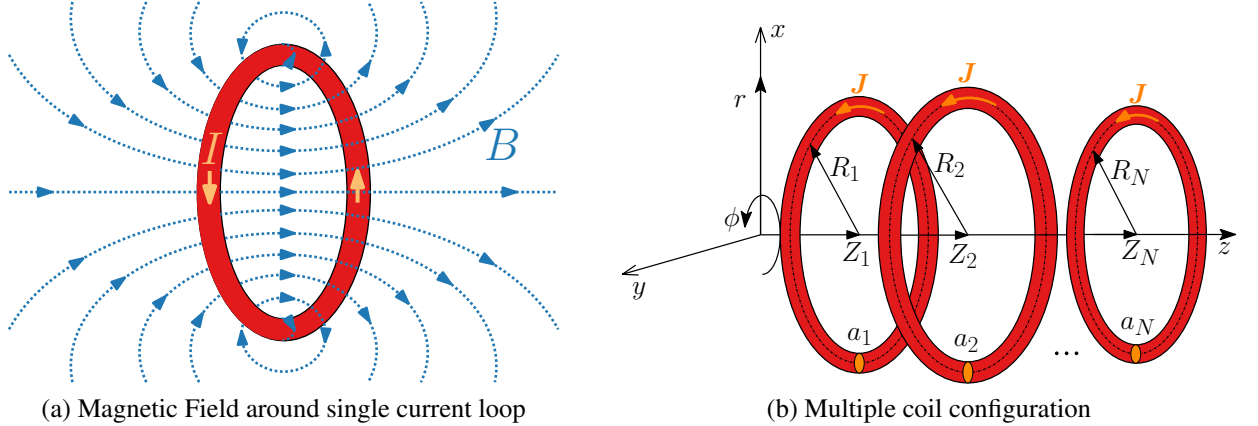


Figure 3: Single current loop, representing a lumped mass of coils.

In the simplified model, shown in Figure 3, all transient, eddy current and coupling effects are neglected, as is the mutual inductance between coils. Coil i has a constant cross sectional area a_i , is circular and hence rotationally symmetric and so is best expressed in terms of cylindrical coordinates (r, ϕ, z) and carries a uniform current density $\mathbf{J}^s = J_\phi^s e_\phi$. Then, by an additive application of the Biot-Savart law for a single coil [47], the following relationship can be derived for the field strength along the axis $r = 0$ for N coils placed at different locations (R_i, Z_i)

$$|\mathbf{J}^s| = \sum_i^N \frac{\left((z - Z_i)^2 + R_i^2\right)^{3/2}}{R_i a_i} |\mathbf{B}(0, \phi, z)|, \quad (24)$$

where $\mathbf{B}(0, \phi, z) = B_z(r = 0, z)\mathbf{e}_z$ along this axis, R_i is the radius and Z_i the axial position of the i^{th} current source relative to the scanner's central axes. Provided the aforementioned assumptions are enforced, this relationship can be applied to obtain the current densities that are associated only with the main magnet ($\mathbf{J}^s = \mathbf{J}^{DC}$) or with the gradient coil ($\mathbf{J}^s = \mathbf{J}^{AC}$) from their produced field strengths. In the context of Section 4.2, it also provides a guide as to the ranges of ratios of $|\mathbf{J}^{AC}|/|\mathbf{J}^{DC}|$ and $||\mathbf{B}^{AC}||_{L^\infty(\Omega)} / ||\mathbf{B}^{DC}||_{L^\infty(\Omega)}$ over which the linearised approach is applicable.

In Section 6, we revisit this simplified model for each of the industrially relevant numerical examples presented in [13], where we present the results of this simplified model to the corresponding problems and show the ranges of the ratios 2) and 3) that MRI scanners operate within.

5 Discretisation of the system

In this section, we briefly recall the spatial discretisation in a *hp*-finite element sense and present the spatially discrete system of coupled second order ODEs. We then present the temporal discretisation of the system of equations to allow for solutions in the time domain, before summarising the steps required to solve the coupled non-linear problem by presenting a generalised solution algorithm.

5.1 Spatial discretisation

The spatial discretisation of the linearised system of coupled acousto-magneto-mechanical equations in (5) is extensively covered in [13], where the treatment of the axisymmetric system and far field conditions are also presented. This approach allows for the refinement of both the mesh spacing and the order of the elements. We have previously shown this to be an effective approach, which leads to accurate solutions, for both benchmark eddy current, mechanical and acoustic problems as well as fully coupled MRI configurations [34, 13]. In our current work, we follow the same approach but have also included the use of infinite elements at the far field boundary to better predict the static decay of the magnetic field [48]. The spatially discrete system of second order ODEs obtained for the *non-linear approach* can be expressed as the Newton-Raphson iteration: Find $\delta_q^{[k]} \in \mathbb{R}^{4N}$ at each time $t \in (0, T]$ such that ⁴

$$\mathbf{M}\ddot{\delta}_q^{[k]} + \mathbf{C}^{[k]}\dot{\delta}_q^{[k]} + \mathbf{K}^{[k]}\delta_q^{[k]} = -\mathbf{R}_q^{[k]}, \quad (25a)$$

$$\mathbf{q}^{[k+1]} = \mathbf{q}^{[k]} + \delta_q^{[k]}, \quad (25b)$$

where $\delta_q^{[k]}$ and $\mathbf{q}^{[k]}$ are spatially discrete forms of the continuous variables $\delta_q^{[k]}$ and $\mathbf{q}^{[k]}$ and \mathbf{M} , $\mathbf{C}^{[k]}$, $\mathbf{K}^{[k]}$ and $\mathbf{R}_q^{[k]}$ are the discrete linearised mass, damping and stiffness matrices and residual vector, respectively, which are obtained by discretising the terms in (7) and depend, with the exception of the mass matrix, on the solution at iteration $[k]$. The partial time derivatives of the solution vectors become ordinary time derivatives due to their independence of spatial coordinates.

In a similar manner, the *linearised approach* takes the form: Find $\delta_q^{[k]} \in \mathbb{R}^{4N}$ at each time $t \in (0, T]$ such that

$$\tilde{\mathbf{M}}\ddot{\delta}_q + \tilde{\mathbf{C}}\dot{\delta}_q + \tilde{\mathbf{K}}\delta_q = -\tilde{\mathbf{R}}_q, \quad (26)$$

where \mathbf{q}^{DC} is the vector of discrete solutions to the static problem and $\tilde{\mathbf{M}}$, $\tilde{\mathbf{C}}$, $\tilde{\mathbf{K}}$ and $\tilde{\mathbf{R}}_q$ are the discrete mass, damping and stiffness matrices and the residual vector, respectively, obtained by discretising the terms in (10). In this case, no Newton-Raphson iteration is required.

5.2 Temporal discretisation

There are a considerable number of alternative time integration techniques that could be employed for the temporal integration of (25) and (26), such as Euler schemes [49], trapezoidal schemes [50], and the Newmark method [51]. In this paper, we chose to adopt a second order generalised- α scheme, see [52], to discretise our system of equations. This scheme is designed to allow for tailor-made numerical dissipation in the solution and is of sufficient degree, given the second order nature of (25) and (26). Given the complexity of the coupled system, it is difficult to know the true initial conditions for the full transient problem, when applying a forced excitation. The numerical dissipation of the generalised- α scheme is therefore beneficial as it can be used to damp out any artificial frequencies that pollute the solution. There exists also a number of high order integration schemes, such as backward differentiation formulas [53], explicit Runge-Kutta and leap-frog type methods [54, 55], that allow for higher order accuracies in time and larger time steps, although with increased temporal accuracy comes a significant increase in computational cost. However, for our problem, the required timestep size is dictated by the need to capture the excitation frequency and resonant frequencies of the system (typically in the region of 5000Hz). For this reason, the need for higher order accuracy is significantly outweighed by the requirement of smaller timestep sizes anyway and thus the generalised- α scheme appears a sensible choice.

5.2.1 Generalised- α time integration scheme (2nd order)

In this section, we focus on the development of the temporal discretisation of (25), which can similarly be developed for (26). The implicit form of this scheme evaluates the system of non-linear equations in (25)

⁴Here we have assumed a spatial discretisation consisting of N basis functions with same order elements employed for each field. There are 4N unknowns since, associated with basis functions, we have the degrees of freedom for A_ϕ , $\tilde{u} = \{\tilde{u}_r \ u_z\}^T$ and \hat{p} , in the axisymmetric case, see [13] for details.

at an intermediate time step $t_{n+1-\alpha_f}$ as

$$\ddot{\mathbf{M}}\delta_{q,n+1-\alpha_m}^{[k]} + \mathbf{C}|_{t_{n+1-\alpha_f}}^{[k]}\dot{\delta}_{q,n+1-\alpha_f}^{[k]} + \mathbf{K}|_{t_{n+1-\alpha_f}}^{[k]}\delta_{q,n+1-\alpha_f}^{[k]} = -\mathbf{R}_q|_{t_{n+1-\alpha_f}}^{[k]}, \quad (27)$$

where $\mathbf{C}|_{t_{n+1-\alpha_f}}^{[k]}$, $\mathbf{K}|_{t_{n+1-\alpha_f}}^{[k]}$ and $\mathbf{R}_q|_{t_{n+1-\alpha_f}}^{[k]}$ are evaluated at the intermediate timestep $t_{n+1-\alpha_f}$ and the values of the fields at this timestep are given by

$$\ddot{\mathbf{q}}_{n+1-\alpha_m}^{[k]} = (1 - \alpha_m)\ddot{\mathbf{q}}_{n+1}^{[k]} + \alpha_m\ddot{\mathbf{q}}_n, \quad (28a)$$

$$\dot{\mathbf{q}}_{n+1-\alpha_f}^{[k]} = (1 - \alpha_f)\dot{\mathbf{q}}_{n+1}^{[k]} + \alpha_f\dot{\mathbf{q}}_n, \quad (28b)$$

$$\mathbf{q}_{n+1-\alpha_f}^{[k]} = (1 - \alpha_f)\mathbf{q}_{n+1}^{[k]} + \alpha_f\mathbf{q}_n, \quad (28c)$$

$$t_{n+1-\alpha_f} = (1 - \alpha_f)t_{n+1} + \alpha_f t_n. \quad (28d)$$

The generalised- α scheme, described in [52], expresses $\mathbf{q}_{n+1}^{[k]}$ and $\dot{\mathbf{q}}_{n+1}^{[k]}$ in terms of $\ddot{\mathbf{q}}_{n+1}^{[k]}$, known as an acceleration based formulation. This can be manipulated into a displacement based formulation, where $\dot{\mathbf{q}}_{n+1}^{[k]}$ and $\ddot{\mathbf{q}}_{n+1}^{[k]}$ are expressed in terms of $\mathbf{q}_{n+1}^{[k]}$, as

$$\ddot{\mathbf{q}}_{n+1}^{[k]} = \frac{1}{\beta} \left(\frac{\mathbf{q}_{n+1}^{[k]} - \mathbf{q}_n}{\Delta t^2} - \frac{\dot{\mathbf{q}}_n}{\Delta t} - \left(\frac{1}{2} - \beta \right) \ddot{\mathbf{q}}_n \right), \quad (29a)$$

$$\dot{\mathbf{q}}_{n+1}^{[k]} = \frac{\varsigma}{\beta} \left(\frac{\mathbf{q}_{n+1}^{[k]} - \mathbf{q}_n}{\Delta t} + \left(\frac{\beta}{\varsigma} - 1 \right) \dot{\mathbf{q}}_n + \left(\frac{\beta}{\varsigma} - \frac{1}{2} \right) \Delta t \ddot{\mathbf{q}}_n \right), \quad (29b)$$

where $\varsigma := \frac{1}{2} - \alpha_m + \alpha_f$, $\beta := \frac{1}{4}(1 - \alpha_m + \alpha_f)^2$, $\alpha_m := \frac{2\rho_\infty - 1}{\rho_\infty + 1}$, $\alpha_f := \frac{\rho_\infty}{\rho_\infty + 1}$, Δt is the timestep size and ρ_∞ denotes the user-specified value of the spectral radius in the high frequency limit⁵.

5.2.2 Predictor-multi-corrector step

The eventual aim of this formulation is to handle fully coupled non-linear problems and employ an iterative procedure at each timestep to fully resolve the solution. Iterative procedures require a prediction of the solution field to compute a converged solution. Therefore, to allow for the robust treatment of the solution at each timestep the introduction of a predictor-corrector algorithm, similar to those proposed in [56], is required. The prediction step [$k = 0$], based on a initial guess of the displacement field $\mathbf{q}_{n+1}^{[0]}$, is defined as

$$\ddot{\mathbf{q}}_{n+1}^{[0]} = \frac{1}{\beta} \left(\frac{\mathbf{q}_{n+1}^{[0]} - \mathbf{q}_n}{\Delta t^2} - \frac{\dot{\mathbf{q}}_n}{\Delta t} - \left(\frac{1}{2} - \beta \right) \ddot{\mathbf{q}}_n \right), \quad (30a)$$

$$\dot{\mathbf{q}}_{n+1}^{[0]} = \frac{\varsigma}{\beta} \left(\frac{\mathbf{q}_{n+1}^{[0]} - \mathbf{q}_n}{\Delta t} + \left(\frac{\beta}{\varsigma} - 1 \right) \dot{\mathbf{q}}_n + \left(\frac{\beta}{\varsigma} - \frac{1}{2} \right) \Delta t \ddot{\mathbf{q}}_n \right), \quad (30b)$$

where (30b) and (30a) are consistent with (29a) and (29b) respectively. In other words both the velocity and accelerations predictors preserve second-order accuracy, as discussed in [57]. If we return our attention to (29b) and (29a) and substitute the fields at iteration step [$k + 1$], we obtain that the update variables of the first and second order fields are

$$\dot{\delta}_{q,n+1}^{[k]} = \frac{1}{\beta \Delta t^2} \delta_{q,n+1}^{[k]}, \quad (31a)$$

$$\ddot{\delta}_{q,n+1}^{[k]} = \frac{\varsigma}{\beta \Delta t} \delta_{q,n+1}^{[k]}. \quad (31b)$$

⁵Traditionally with the generalised α method, γ is used to refer to the first stability parameter, however, given our formulation reserves γ for the material conductivity, we use instead the alternative symbol ς .

5.2.3 Full discrete non-linear approach

Using the relations between the updates, in (31), we may rewrite the discrete system, in (27), in terms of the update in the zeroth order solution vector $\delta_{q|n+1}^{[k]}$ at time t_{n+1} as the following Newton-Raphson procedure: Find $\delta_{q|n+1}^{[k]} \in \mathbb{R}^{4N}$ at each time $t \in (0, T]$ such that

$$\left(\frac{(1 - \alpha_m)}{\beta \Delta t^2} \mathbf{M} + \frac{\varsigma(1 - \alpha_f)}{\beta \Delta t} \mathbf{C}|_{t_{n+1-\alpha_f}}^{[k]} + (1 - \alpha_f) \mathbf{K}|_{t_{n+1-\alpha_f}}^{[k]} \right) \delta_{q|n+1}^{[k]} = -\mathbf{R}_{q|n+1}^{[k]}, \quad (32a)$$

$$\mathbf{q}_{n+1}^{[k+1]} = \mathbf{q}_{n+1}^{[k]} + \delta_{q|n+1}^{[k]}, \quad (32b)$$

which is iterated over $[k]$ until $|\mathbf{R}_{q|n+1}^{[k]}| < \text{TOL}$.

5.2.4 Fully discrete linearised approach

The fully discrete version of (27) for the *linearised approach* is similarly expressed as: Find $\delta_{q|n+1} \in \mathbb{R}^{4N}$ at each time $t \in (0, T]$ such that

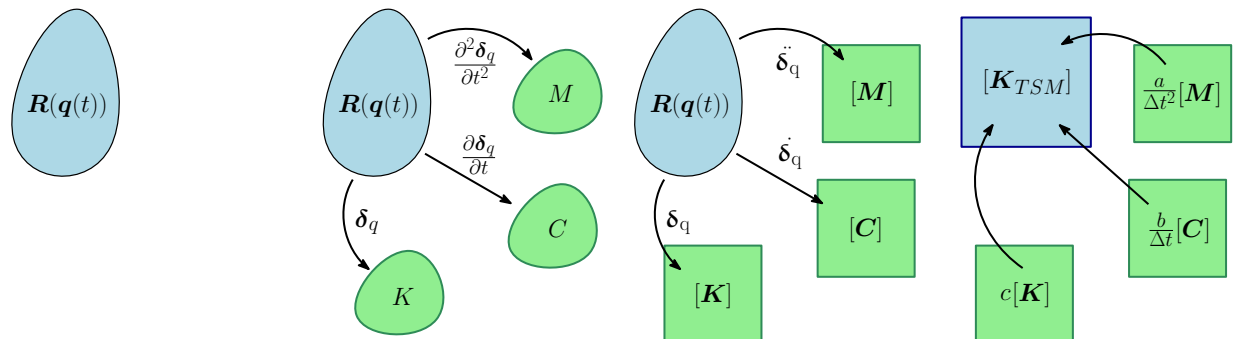
$$\left(\frac{(1 - \alpha_m)}{\beta \Delta t^2} \tilde{\mathbf{M}} + \frac{\varsigma(1 - \alpha_f)}{\beta \Delta t} \tilde{\mathbf{C}} + (1 - \alpha_f) \tilde{\mathbf{K}} \right) \delta_{q|n+1} = -\tilde{\mathbf{R}}_{q|n+1}, \quad (33)$$

where the system matrices $\tilde{\mathbf{M}}$, $\tilde{\mathbf{C}}$ and $\tilde{\mathbf{K}}$ are independent of the previous temporal solutions and $\tilde{\mathbf{R}}_{q|n+1}$ depends only on the evaluation of \mathbf{J}^{AC} at time level $t_{n+1-\alpha_f}$ and so can be solved in a single step, which is a simplified version of (32).

5.3 Solution algorithm

A general algorithm for computing the transient variation in the fields for both the *non-linear* and *linearised approaches*, proposed above, under a generalised- α scheme is summarised in the following algorithm, where for the latter approach no iterations are required and so $N_k = 0$, thus rendering the predictor-multi-corrector algorithm to a predictor-corrector.

Figure 4 summarises the steps required to construct the discretised Newton-Rapshon iterative scheme in (32) from the transient non-linear transmission problem (1)



(a) Residual weak form of coupled non-linear system (b) Linearisation of the non-linear system (c) Discretisation of the directional derivatives (d) Temporal discretisation and building system matrix

Figure 4: Summary of steps to solving transient non-linear system.

Algorithm 1 Algorithm to compute the time variation of the coupled transient system

- 1: Define the initial conditions of the fields $\mathbf{q}_0, \dot{\mathbf{q}}_0, \ddot{\mathbf{q}}_0$ from (3)
- 2: **for** $n = 0, 1, 2 \dots N_{\Delta t}$ **do** ▷ Number of timesteps $N_{\Delta t}$
- 3: Predict the solution at the current timestep $\mathbf{q}_{n+1}^{[0]}, \dot{\mathbf{q}}_{n+1}^{[0]}, \ddot{\mathbf{q}}_{n+1}^{[0]}$ from (30)
- 4: **while** $|\mathbf{R}_q| < \text{TOL}; k = 0, 1, 2 \dots N_k$ **do** ▷ Number of iterations N_k
- 5: Compute the fields $\mathbf{q}_{n+1-\alpha_f}^{[k]}, \dot{\mathbf{q}}_{n+1-\alpha_f}^{[k]}$ and $\ddot{\mathbf{q}}_{n+1-\alpha_m}^{[k]}$ at $t_{n+1-\alpha_f}$ from (28)
- 6: Solve the linear system (32) or (33) for the solution update

$$\mathbf{K}_{TSM}^{[k]} \boldsymbol{\delta}_{q,n+1}^{[k]} = -\mathbf{R}_q|_{t_{n+1-\alpha_f}}^{[k]},$$

where $\mathbf{K}_{TSM}^{[k]} = \left(\frac{(1-\alpha_m)}{\beta \Delta t^2} \mathbf{M} + \frac{\varsigma(1-\alpha_f)}{\beta \Delta t} \mathbf{C}|_{t_{n+1-\alpha_f}}^{[k]} + (1-\alpha_f) \mathbf{K}|_{t_{n+1-\alpha_f}}^{[k]} \right)$ for the *non-linear approach* and $\mathbf{K}_{TSM} = \left(\frac{(1-\alpha_m)}{\beta \Delta t^2} \tilde{\mathbf{M}} + \frac{\varsigma(1-\alpha_f)}{\beta \Delta t} \tilde{\mathbf{C}} + (1-\alpha_f) \tilde{\mathbf{K}} \right)$ and \mathbf{R}_q is replaced by $\tilde{\mathbf{R}}_q$ for the *linearised approach*

- 7: Update the solution fields

$$\begin{aligned} \mathbf{q}_{n+1}^{[k+1]} &= \mathbf{q}_{n+1}^{[k]} + \boldsymbol{\delta}_{q,n+1}^{[k]} \\ \dot{\mathbf{q}}_{n+1}^{[k+1]} &= \dot{\mathbf{q}}_{n+1}^{[k]} + \frac{\varsigma}{\beta \Delta t} \boldsymbol{\delta}_{q,n+1}^{[k]} \\ \ddot{\mathbf{q}}_{n+1}^{[k+1]} &= \ddot{\mathbf{q}}_{n+1}^{[k]} + \frac{1}{\beta \Delta t^2} \boldsymbol{\delta}_{q,n+1}^{[k]} \end{aligned}$$

- 8: **end while**

- 9: **end for**
-

6 Numerical examples

In this section, we discuss two benchmark MRI test problems in order to prove the conjectures presented in Section 4. We study the linearity of the fields for a range of different current density values in the coils to determine the validity of the *linearised approach*.

6.1 Test magnet problem

First, we consider solutions to the industrially relevant test magnet problem, which was previously presented in [13] as the “Siemens benchmark problem”. The conducting region Ω_c of the test magnet consists of three metallic shields, known as the Outer Vacuum Chamber (OVC) Ω_c^{OVC} , $77^\circ K$ radiation shield Ω_c^{77K} and $4^\circ K$ helium vessel Ω_c^{4K} , each with different material parameters ($\gamma, \mu, \lambda, G, \rho$). The exact geometries and material parameters of the conducting components are commercially sensitive and as such are not displayed in this paper. By choosing to study only the Z-gradient coils and noting that the currents in the main coils and geometry of the conducting components are rotationally symmetric, the problem may be reduced to an axisymmetric description and solved in cylindrical coordinates (r, ϕ, z) on the meridian plane Ω^m . The full 3D representation of this simplified MRI scanner is depicted in Figure 5.

A pair of main magnet coils, each with a static current source $\mathbf{J}^{DC} = J_\phi^{DC}(r, z)\mathbf{e}_\phi$, are located on the outside of the three shields and a pair of Z-gradient magnet coils, each with alternating current source $\mathbf{J}^{AC}(t) = J_\phi^{AC}(t, r, z)\mathbf{e}_\phi$, are located within the imaging bore, both of which are assumed as Biot-Savart conductors and are located in free space. Realistic excitations of the gradient coil are non-sinusoidal in nature, however for the purposes of comparison between the *linearised* and *non-linear approaches* we restrict ourselves to sinusoidal excitations, where the current density is described by $J_\phi^{AC}(t) = \text{Re} \left(|J_\phi^{AC}| e^{i\omega t} \right)$. We consider several frequencies of excitation of $\omega = 2\pi[1000, 1500, 2000]\text{rad/s}$, which lie outside of the resonance region of $\omega \geq 2\pi[3500]$, predicted in [34, 13]. The magnitude of the static $|J_\phi^{DC}|$ and gradient

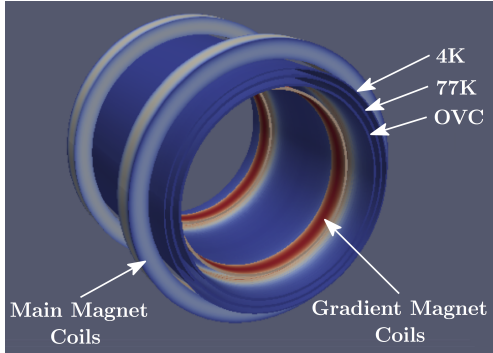


Figure 5: Test magnet problem: Components of the simplified geometry.

current sources $|J_\phi^{AC}|$ to be considered are obtained from manufacturer's data [6, 7, 8]. This data quotes the maximum capable flux density on the central axis of the imaging bore ($r = 0$) and in order to obtain the corresponding current densities we have used the model described in Section 4.3, the results of which are summarised, for key clinical field strengths, in Table 1.

Main Coil		Gradient Coil	
$\max \mathbf{B}_{z=0}^{DC} $ [T]	$ J_\phi^{DC} $ [$\times 10^{-6}$ A/m ²]	$\max \mathbf{B}_{z=0}^{AC} $ [$\times 10^{-3}$ T/m]	$ J_\phi^{AC} $ [$\times 10^{-6}$ A/m ²]
1.5	218.35	30	4.70
3	436.70	80	12.53
11.7	1703.10	100	15.66

Table 1: Test magnet problem: Typical values of the current densities in static and gradient coils and ranges of static and gradient field strengths from manufacturers data [6, 7, 8].

Given criteria 2) and 3) in Section 4.2, the greatest non-linearity should appear for a magnet with weakest static field of 1.5T and strongest gradient field of 100×10^{-3} T/m. This would result in a ratio between the static and gradient current density values of $|J_\phi^{AC}| / |J_\phi^{DC}| \approx 7.2\%$ for this problem. We therefore study the two *approaches* across a range of current density ratios of $|J_\phi^{AC}| / |J_\phi^{DC}| = [5, 10, 15, 20]\%$ to provide a rigorous test of the *linearised approach* for applications of higher levels of non-linearity than current MRI scanners are capable of. The problem is subject to the following boundary conditions: we fix the Dirichlet boundaries of the conductors to $\mathbf{u}^D = \mathbf{0}$ to fix the conductors in space, as in Section 2, and we set the value of the magnetic vector potential on the outer boundary to $A_\phi = 0$ due to the eddy current decay. The initial conditions of the problem are defined by those described in Section 2.3.

We treat this problem computationally for both the *linearised* and *non-linear approaches*. We truncate the non-conducting free space region, comprised of air, and create the domain Ω^m , which is the same as in [13]. In terms of spatial discretisation, we analyse the solution for a single unstructured mesh of 2,842 triangles of maximum size $h = 0.25$ m, but with substantial refinement in the conductors Ω_c^m , resulting in 570 elements in Ω_c^m . The mesh parameters used are the same as in [13], however, due to improvements in the mesh generator used [58] resulted in a better distribution of elements and hence fewer elements. We apply a single layer of 18 infinite elements on the outer boundary of Ω^m to resolve the static decay of the magnetic field, so that the boundary condition $A_\phi = 0$ is effectively imposed at infinity. We consider p -refinement for elements of order $p = [1, 2, 3, 4, 5]$. The temporal discretisation used to resolve these waves are studied for a timestep size of $\Delta t = 2\pi/(\omega N_{\Delta t})$, where we vary the number of points per wavelength of the excitation frequency $N_{\Delta t} = [10, 20, 30, 40]$. The spectral radius of the α -scheme time integrator ρ_∞ allows for damping of certain frequency regimes. For $\rho_\infty = 1$ the amplitude of the wave is fully preserved and no damping of any high frequencies is introduced. For $\rho_\infty = 0$ the scheme is fully

dissipative and higher frequency waves are completely damped, however, the damping of physical modes also occurs. Given that we wish to recover only physical modes in our problem, we therefore chose the value of $\rho_\infty = 0.8$, to allow for numerical damping of any non-physical high frequencies induced through the forcing, whilst still preserving the physical lower frequency waves.

Solutions to this problem are obtained by applying Algorithm 1 for both the *non-linear* and *linearised approaches* across the range of current densities and excitation frequencies discussed.

6.1.1 Convergence study in outputs of interest

We consider quantities of industrial interest for both the mechanical and electromagnetic fields. For the electromagnetic field we are concerned with the output power dissipation in the conducting components $P_{\Omega_c}^o$ and for the mechanical field we are concerned with the kinetic energy of the conducting components $E_{\Omega_c}^k$. The formal definition of these quantities in a full time domain description, where the quantities are averaged over the time period T of excitation frequency, are

$$P_{\Omega_c}^o(t, \mathbf{A}) = \frac{1}{T} \int_t^{t+T} \int_{\Omega_c} \gamma \left| \frac{\partial \mathbf{A}}{\partial t} \right|^2 d\Omega dt, \quad E_{\Omega_c}^k(t, \mathbf{u}) = \frac{1}{T} \int_t^{t+T} \frac{1}{2} \int_{\Omega_c} \rho \left| \frac{\partial \mathbf{u}}{\partial t} \right|^2 d\Omega dt, \quad (35)$$

which reduce, in a time harmonic representation, to

$$P_{\Omega_c}^o(\omega, \mathbf{A}) = \frac{1}{2} \int_{\Omega} \gamma \omega^2 |\mathbf{A}(\omega)|^2 d\Omega, \quad E_{\Omega_c}^k(\omega, \mathbf{u}) = \frac{1}{4} \int_{\Omega} \rho \omega^2 |\mathbf{u}(\omega)|^2 d\Omega, \quad (36)$$

where $\mathbf{A}(\omega)$ and $\mathbf{u}(\omega)$ are the complex amplitudes of their respective fields as $\mathbf{A}(t) = \text{Re}(\mathbf{A}(\omega)e^{i\omega t})$ and $\mathbf{u}(t) = \text{Re}(\mathbf{u}(\omega)e^{i\omega t})$, as described in [13]. To compute these quantities for the test magnet problem, using either the transient solutions obtained by the *linearised* or *non-linear approaches*, Algorithm 1 is run at specific $N_{\Delta t}$, Δt , ρ_∞ for a sufficiently long time until the field responses reach steady state. Equation 35 is then applied over the time period of excitation T .

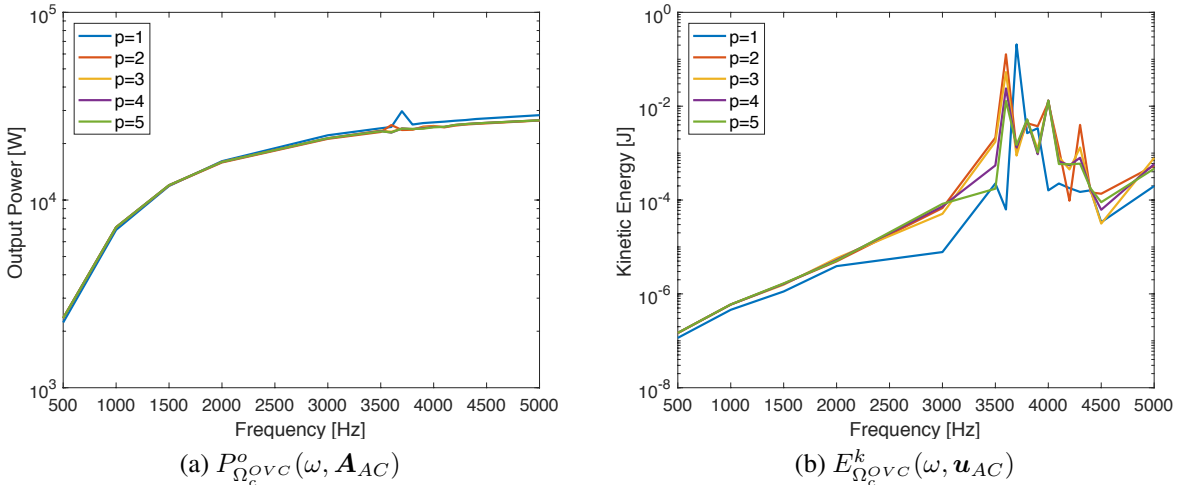


Figure 6: Test magnet problem: Output power (left) and kinetic energy (right) of the OVC Ω_c^{OVC} for element order $p = [1, 2, 3, 4, 5]$.

In order to determine suitable spatial resolution in the solution we perform a p -refinement study. We apply Algorithm 1 for $N_{\Delta t} = 30$, $\rho_\infty = 0.8$ using the *linearised approach* to compute the output power and kinetic energy across the frequency spectrum for $\omega \leq 2\pi[5000]$, the results of which are illustrated in Figure 6. For $p \leq 3$ the computed curves, illustrated in Figure 6, do not match one another and so the results have not yet reached convergence. The curves for $p = 4$ and $p = 5$, however, are practically indistinguishable for both the output power and kinetic energy and suggests that for elements of order

$p = 4$ the results are sufficiently converged. We hence decide to adopt elements of $p = 4$ for all subsequent computations of this problem on the mesh specified previously.

A similar study to determine the required timestep size was also carried out, where a range of number of time steps per wavelength $N_{\Delta t} = [10, 20, 30, 40]$ for $p = 4$ elements were studied. The results suggest that $N_{\Delta t} = 30$ offers sufficient temporal resolution to capture the amplitudes of the dominant frequency as well as frequencies twice the dominant frequency 2ω . The importance of this frequency doubling will be explained later in Section 6.1.3. Thus for an excitation frequency of $\omega = 2\pi[1000]$ the timestep size $\Delta t = 3.333 \times 10^{-5}$ s, for $\omega = 2\pi[1500]$ the $\Delta t = 2.222 \times 10^{-5}$ s and for $\omega = 2\pi[2000]$ the $\Delta t = 1.667 \times 10^{-5}$ s. For the full set of results see [59].

Using these parameters, in Section 6.1.4, we compute the quantities in (35) by applying Algorithm 1 for the *linearised* and *non-linear approaches* in the time domain and compare them with our previous frequency domain solver [13]. However, first we consider the results for the *linearised* and *non-linear approaches* for transient electromagnetic and mechanical fields.

6.1.2 Electromagnetic field

Firstly, in order to perform comparisons between the *linearised* and *non-linear approaches* we compare the transient response of the magnetic field for both *approaches*. Given that the output power of the conductors $P_{\Omega_c}^o$, described above, is driven by the temporal derivative of the magnetic vector potential $\partial \mathbf{A} / \partial t$, we measure and compare the response of this field.

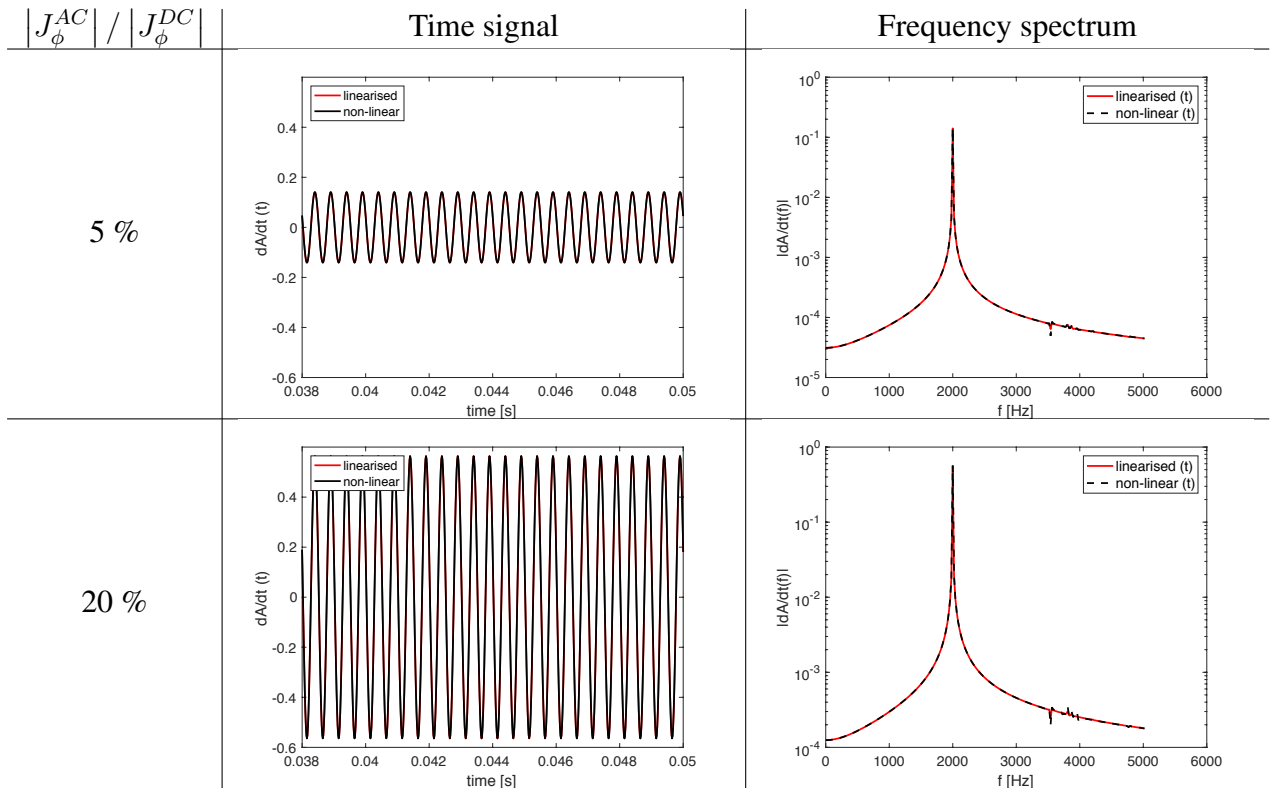


Figure 7: Test magnet problem: Time signals and corresponding FFTs of $\partial \mathbf{A} / \partial t$ for both the *linearised* (red line) and *non-linear approaches* (black line), for various values of $|J_\phi^{AC}| / |J_\phi^{DC}|$ subject to a $\omega = 2\pi[2000]$ rad/s sinusoidal excitation.

Figure 7 summarises the transient results of both *approaches* for the $\omega = 2\pi[2000]$ rad/s sinusoidal excitation. The graphs in the left hand column plot the time signal obtained from both the *linearised approach* (in red) and *non-linear approach* (in black). The right hand column plots the corresponding frequency spectrum of the signal, obtained by performing Fast Fourier Transforms (FFTs). We can see from this figure that the *linearised approach* provides an accurate approximation of the magnetic vector

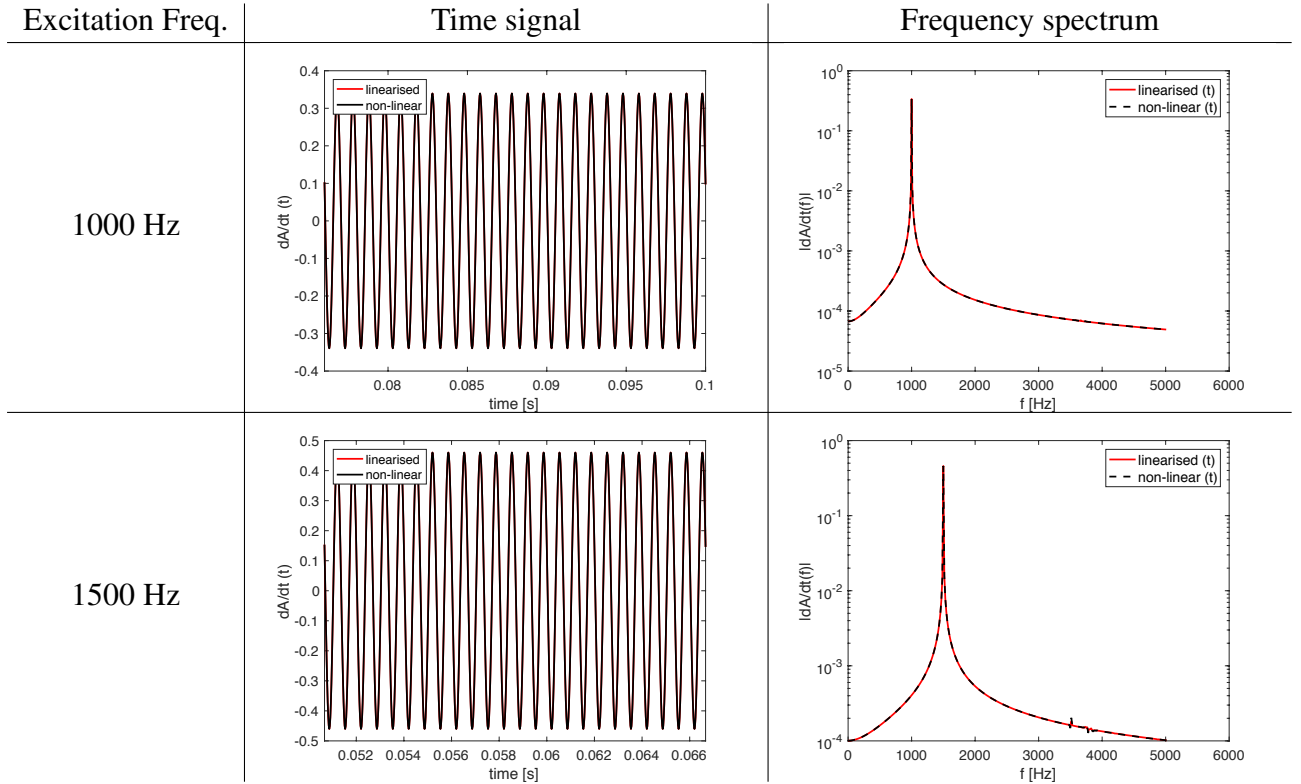


Figure 8: Test magnet problem: Time signals and corresponding FFTs of $\partial \mathbf{A} / \partial t$ for both the *linearised* and *non-linear approaches*, for $|J_\phi^{AC}| / |J_\phi^{DC}| = 20\%$ subject to various frequencies of excitation.

potential across the full range of current density ratios. The magnitude of the frequencies across the spectrum are almost identical and the *linearised approach* is even capable of capturing all the fundamental frequencies, around $\omega = 2\pi[3500 - 4000]\text{rad/s}$.

Figure 8 plots the transient response and corresponding frequency spectrum for a current density ratio of $|J_\phi^{AC}| / |J_\phi^{DC}| = 20\%$ and a range of excitation frequencies. These plots again illustrate the agreement between the *linearised* and *non-linear approaches* for different excitation frequencies.

6.1.3 Mechanical field

We now compare the response of the mechanical field for both the *linearised* and *non-linear approaches*. Given that the kinetic energy of the conductors $E_{\Omega_c}^k$, described in Section 6.1.1, is driven by their mechanical velocity $\partial \mathbf{u} / \partial t$, we measure and compare the response of this field.

Figure 9 summarises the transient results of both *approaches* for the $\omega = 2\pi[1000]\text{rad/s}$ sinusoidal excitation. The graphs in the left hand column plot the time signal obtained from both the *linearised approach* (in red) and *non-linear approach* (in black). From the plots it appears as though the two *approaches* offer good agreement, especially when looking at the time signals. However, in the frequency spectrum there appears to be an extra frequency at $\omega = 2\pi[2000]\text{rad/s}$ that is picked up in the *non-linear approach*, but not in the *linearised approach*. This term appears due to the non-linearity in the Maxwell stress tensor (2), which we can observe is quadratic in the magnetic field. From a decomposition of the magnetic field into static and dynamic components, as shown in Section 2.2, it can be shown that this non-linear term comprises of a product of the dynamic component of the field with itself, which disappears in the *linearised approach*. This term causes a frequency doubling effect, in other words it results in a component of excitation of the mechanical field that is double the frequency of the AC currents. So for a $\omega = 2\pi[1000]\text{rad/s}$ wave, as in Figure 10, an excitation at $\omega = 2\pi[2000]\text{rad/s}$ would also appear, which matches exactly with the results obtained. However, from Figure 10, it is clear that the magnitude of this term is far smaller

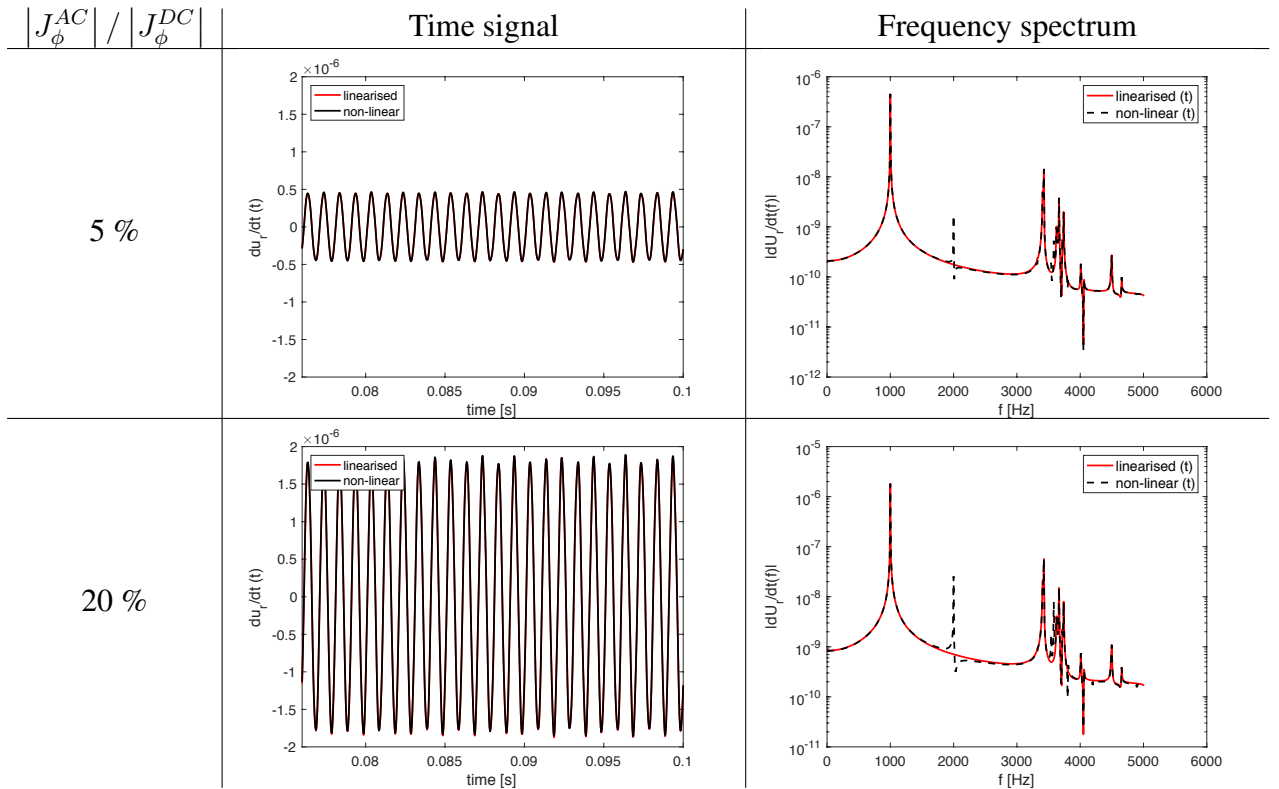


Figure 9: Test magnet problem: Time signals and corresponding FFTs of $\partial u_r / \partial t$ for both the *linearised* and *non-linear approaches*, for various values of $|J_\phi^{AC}| / |J_\phi^{DC}|$ subject to a $\omega = 2\pi[1000]$ rad/s sinusoidal excitation.

than that of the amplitude associated with the exciting frequency and thus has little effect on the solution. As the ratio of the current densities increases so too does the magnitude of this term. However, even for a ratio of 20% the magnitude is still several orders smaller than the main excitation and smaller also than the most dominant resonant frequencies. Thus the magnitude of this doubled frequency component provides a useful measure in determining the non-linearity of the problem.

Figure 10 plots the transient response and corresponding frequency spectrum for a current density ratio of $|J_\phi^{AC}| / |J_\phi^{DC}| = 20\%$ and a range of excitation frequencies. We see from these plots that for the AC current frequencies of 1500Hz the agreement between the two *approaches* results in almost indistinguishable time signals. However, for the $\omega = 2\pi[2000]$ rad/s AC currents differences in the time signal become more visible. This is because the doubled frequency excitation component of 4000Hz lies within the resonance region. When exciting close to the resonance region the problem results in matrices of high condition numbers, which are close to singular. Consequently, the tangent stiffness matrix inversion becomes more challenging and less reliable and, as a result, can lead to differences in the amplitudes across the frequency spectrum. Despite this effect however, the differences in the time signal are still very small and the characteristics of the system and prediction of the resonance region remain well captured by the *linearised approach*.

6.1.4 Comparison of *linearised* and *non-linear approaches*

To benchmark the accuracy of the solution from the *linearised approach* with the *non-linear approach*, we compare the computation of the outputs of interest for the two *approaches*, presented in Section 6.1.1, across the range of frequencies $\omega \leq 2\pi[5000]$ rad/s. Figure 11 illustrates the outputs of interest computed by the *linearised approach* in both frequency and time domain and the *non-linear approach* in time domain, using the definitions in (35) and (36) for a current density ratio of $|J_\phi^{AC}| / |J_\phi^{DC}| = 10\%$.

Using the frequency domain approach, described in [13], the outputs of interest $P_{\Omega_c}^o$ and $E_{\Omega_c}^k$ can be

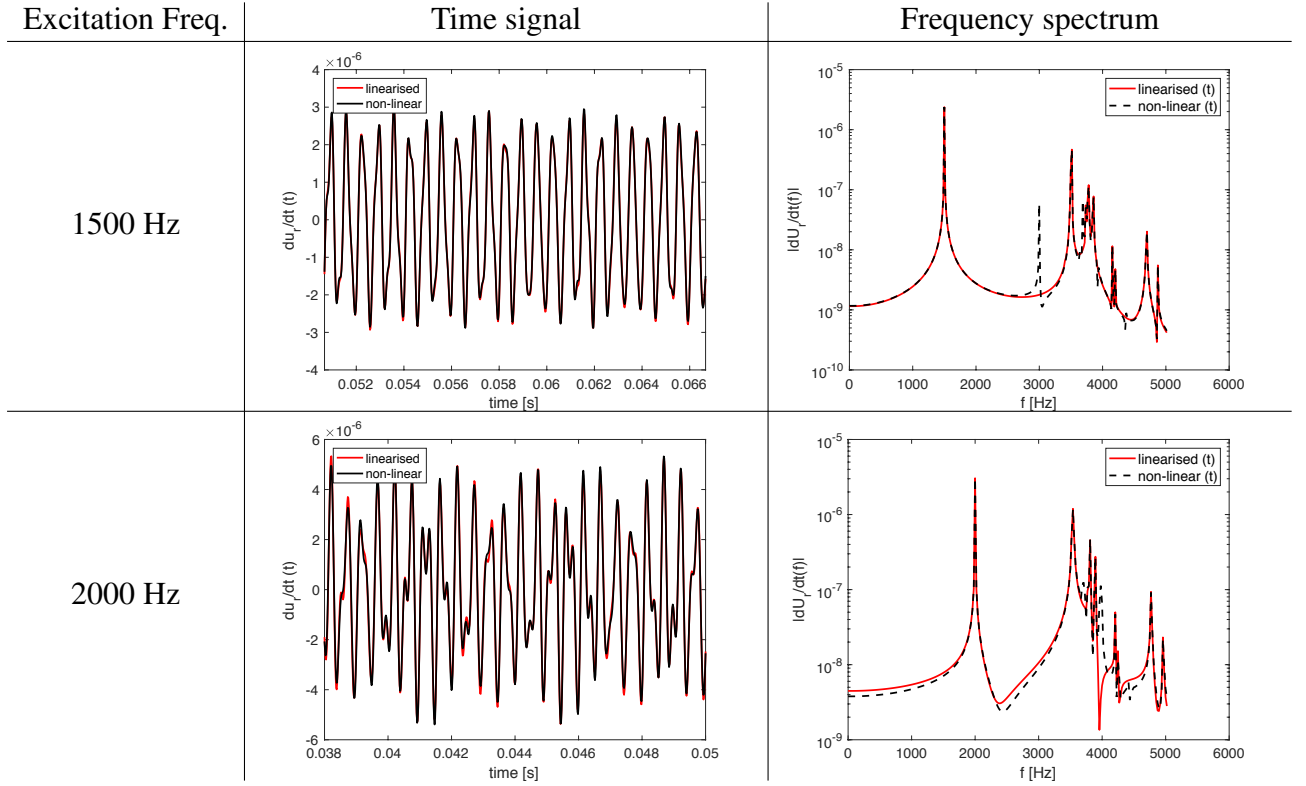


Figure 10: Test magnet problem: Time signals and corresponding FFTs of $\partial u_r / \partial t$ for both the *linearised* and *non-linear approaches*, for $|J_\phi^{AC}| / |J_\phi^{DC}| = 20\%$ subject to various frequencies of excitation.

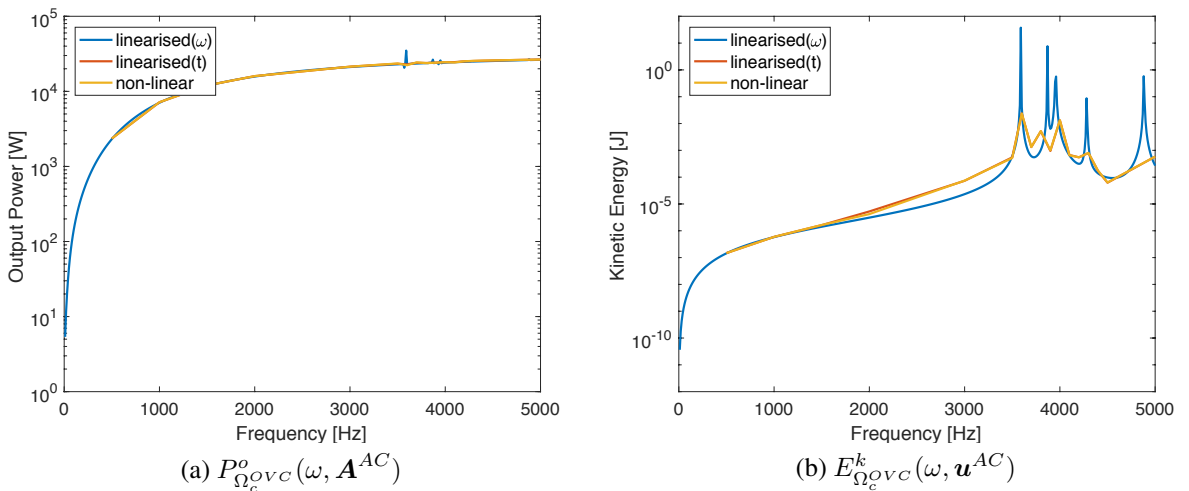


Figure 11: Test magnet problem: Computation of the Output Power (left) and Kinetic Energy (right) of the OVC Ω_c^{OVC} for both the *linearised approach* in time and frequency domain as well as the *non-linear approach*.

directly computed for a given excitation frequency. Whereas, in the time domain we must run the time solver until steady state is obtained and then apply the definition in (35) across a time period. Due to the increased computational cost of computing the outputs of interest for transient solutions, we have chosen to compute them for a coarser frequency sweep compared to the frequency domain results. Figure 11a plots the output power in the OVC $P_{\Omega_{OVC}}^o(\omega, \mathbf{A}^{AC})$ and Figure 11b plots the kinetic energy in the OVC $E_{\Omega_{OVC}}^k(\omega, \mathbf{A}^{AC})$. For the results of the other shields, which show similar agreement, see [59]. From the plots, the curves produced by the *linearised* and *non-linear approaches* are almost indistinguishable across the frequency spectrum which suggests that the *linearised approach* provides a very accurate approximation to the full *non-linear approach* across the full spectrum for $|J_\phi^{AC}| / |J_\phi^{DC}| = 10\%$ for the two outputs of interest. In fact, given that the individual fields, analysed in Sections 6.1.2 and 6.1.3, also show very good agreement for $|J_\phi^{AC}| / |J_\phi^{DC}| = 20\%$, we can hypothesise this to be the case also for the outputs of interest as they are directly related.

We now compare the displacements of the mechanical shields by plotting the displacements of the OVC, in three dimensions, at interesting instances of the time signal for the radial velocity $\partial u_r / \partial t$ computed for the case of $|J_\phi^{AC}| / |J_\phi^{DC}| = 20\%$ and $\omega = 2\pi(2000)\text{rad/s}$ in Figure 12. The chosen time instances across the time signal are plotted, where the difference in the mechanical velocities between the *linearised* and *non-linear approaches* is noticeable. The contour plots of the displacement fields are all scaled such that the colour maps between the *linearised* and *non-linear approaches* are the same. The displacements in Figure 12 are scaled by several orders of magnitude to show visually the displacement shapes of the shield. We can see that for all snapshots the differences between the two *approaches* are almost indistinguishable. This suggests that even for $|J_\phi^{AC}| / |J_\phi^{DC}| = 20\%$ and an excitation frequency of $\omega = 2\pi(2000)\text{rad/s}$, where the doubled frequency component of $\omega = 2\pi(4000)\text{rad/s}$ resides in the resonance region, see Section 6.1.3, that the *linearised approach* provides accurate and comparable results to the full *non-linear approach*. For the results of the other shields see [59].

The average computational timings, per timestep, for the two *approaches* across a range of different element orders p are summarised in Table 2. The comparison between the computational timings of the two *approaches* suggests that the *linearised approach* is orders of magnitude more efficient in terms of computational cost than the *non-linear approach*. For low order $p = 1$ elements the *linearised approach* requires 383 times less computational effort than the *non-linear approach*. Whereas, for higher order $p = 5$ elements the *linearised approach* requires 164 times less computational effort than the *non-linear approach*. This speed-up factor appears to offer an inverse exponential behaviour with p , which is due to the higher requirement on the solver for higher order elements. Nevertheless, the computational timings displayed in the table suggest that the *linearised approach* offers orders of magnitude increase in computational efficiency over the *non-linear approach*.

<i>linearised approach</i>		<i>non-linear approach</i>		
p	Computational time [s]	p	Computational time [s]	Speed-up
1	0.037	1	14.175	383
2	0.181	2	49.327	273
3	0.489	3	116.830	239
4	1.150	4	206.424	179
5	2.187	5	358.914	164

Table 2: Test magnet problem: Average Computational times per timestep of the *linearised* and *non-linear approaches* for specific element order $p = [1, 2, 3, 4, 5]$.

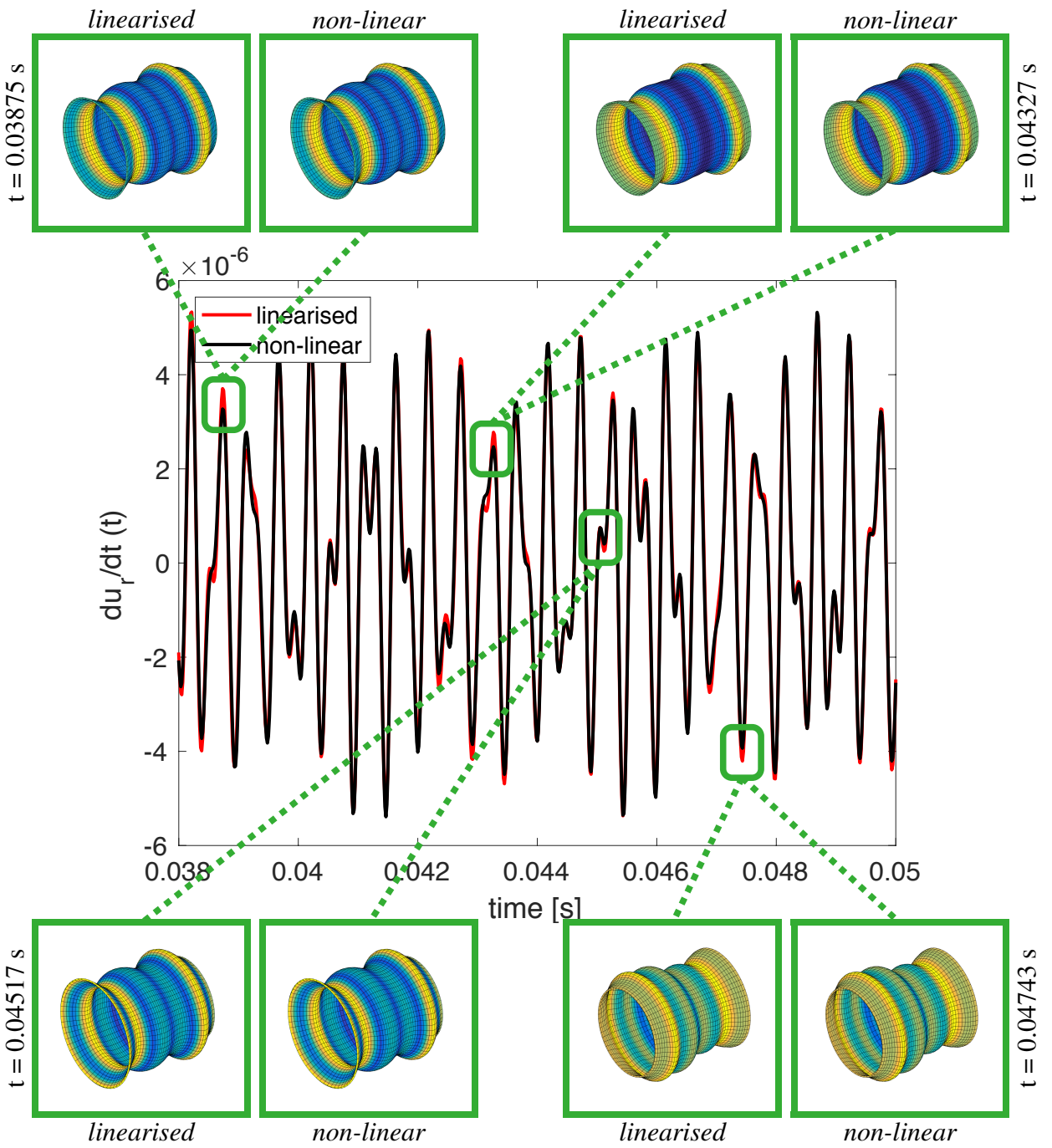


Figure 12: Test magnet problem: Comparison between the *linearised* and *non-linear approaches* for displacements of the OVC at different times for $|J_\phi^{AC}| / |J_\phi^{DC}| = 20\%$ and $\omega = 2\pi(2000)\text{rad/s}$.

6.2 Realistic magnet problem

We now consider a more realistic problem that represents, very accurately, the sorts of MRI scanner designs currently used in clinical operation. The geometry is illustrated in Figure 13a. This problem consists of a similar construction to the previous problem, where the conducting region is comprised of the three radiation shields $\Omega_c = \Omega_c^{OVC} \cup \Omega_c^{77K} \cup \Omega_c^{4K}$, each with different material parameters ($\gamma, \mu, \lambda, G, \rho$). The geometry of the radiation shields, however, is more complex and their topology represents that of closed cylindrical shells of trapezoidal cross section, with curved face end sections. However, despite the increased complexity in topology, the geometry is still cylindrical and can be treated as axisymmetric. Again, the exact geometries and material parameters of the conducting components are commercially sensitive and as such are not displayed in this paper. The configuration of the static main coil consists of the same block cross section as the test magnet problem, but contains more sets of coils including also a set of secondary coils, which act to minimise the magnetic stray field by reversing the polarity of the magnetic field. The gradient coils of this problem represent a far more realistic Z-gradient coil structure, which also contains a set of primary and secondary coils for shielding. The coils are sourced in the same way as the test magnet problem. The cross section of this problem, projected onto the positive half axisymmetric meridian domain $\Omega^m(r, z \geq 0)$, is illustrated in Figure 13b.

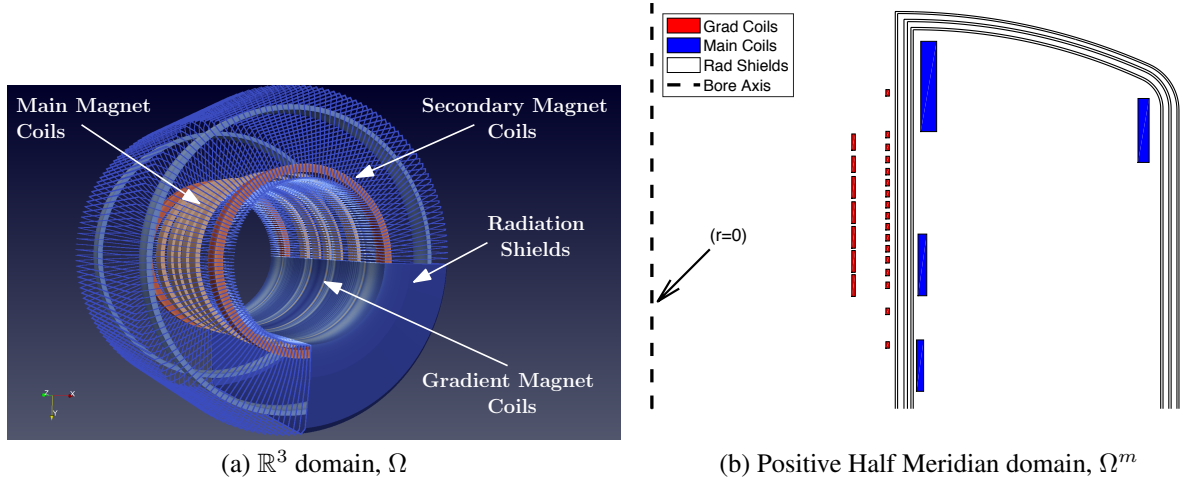


Figure 13: Realistic magnet problem: components of the simplified geometry.

Given criteria 2) and 3) in Section 4.2, the greatest non-linearity is expected appear for a magnet with weakest static field of 1.5T and strongest gradient field of 100×10^{-3} T/m. This would result in a ratio between the static and gradient current density values of $|J_\phi^{AC}| / |J_\phi^{DC}| \approx 12.3\%$ for this problem. We therefore study the two *approaches* for an extreme case of a current density ratio of $|J_\phi^{AC}| / |J_\phi^{DC}| = 15\%$ to rigorously test the *linearised approach*. The form of the excitation of J_ϕ^{AC} is as described in Section 6.1.

In terms of boundary conditions, we truncate the non-conducting free space region, comprised of air, and create the domain Ω^m and apply those similar to the test magnet problem, whereby we set the Dirichlet boundaries of the conductors to $\mathbf{u}^D = 0$ to fix the conductors in space. We also set the magnetic vector potential to be $A_\phi = 0$ on the outer boundary.

In terms of spatial discretisation, we analyse the solution for an unstructured mesh of 19,218 triangles of maximum size $h = 0.25$ m, but with substantial refinement in the conductors Ω_c^m , resulting in 4,085 elements in Ω_c^m . We then apply a single layer of 40 quadrilateral finite elements on the outer boundary of Ω^m to resolve the static decay of the magnetic field. Having carried out similar convergence studies to those presented for the test magnet problem, we have chosen use order $p = 4$ elements, $N_{\Delta t} = 30$ timesteps per excitation frequency ω and set $\rho_\infty = 0.8$ for the solutions to this problem.

We now compare the displacements of the mechanical shields by plotting the velocity magnitude of the system across the time signal using both *approaches* for $|J_\phi^{AC}| / |J_\phi^{DC}| = 15\%$ and $\omega = 2\pi(1500)\text{rad/s}$ in Figure 14. Given that the differences in both the time signal and the displaced shapes of the OVC between the two *approaches* are almost indistinguishable, we highlight instead snapshots of the mechanical displacement in the inner OVC shell at various time instances across the time signal for the *linearised approach*. For the full results of the other shields see [59]. We plot the displaced OVC and static magnetic field for the static problem, in Figure 15, and the corresponding gradient fields, at various time instances, in Figure 16. The displacements in Figures 14 15 and 16 are scaled by several orders of magnitude to show visually the displacement shapes of the OVC.

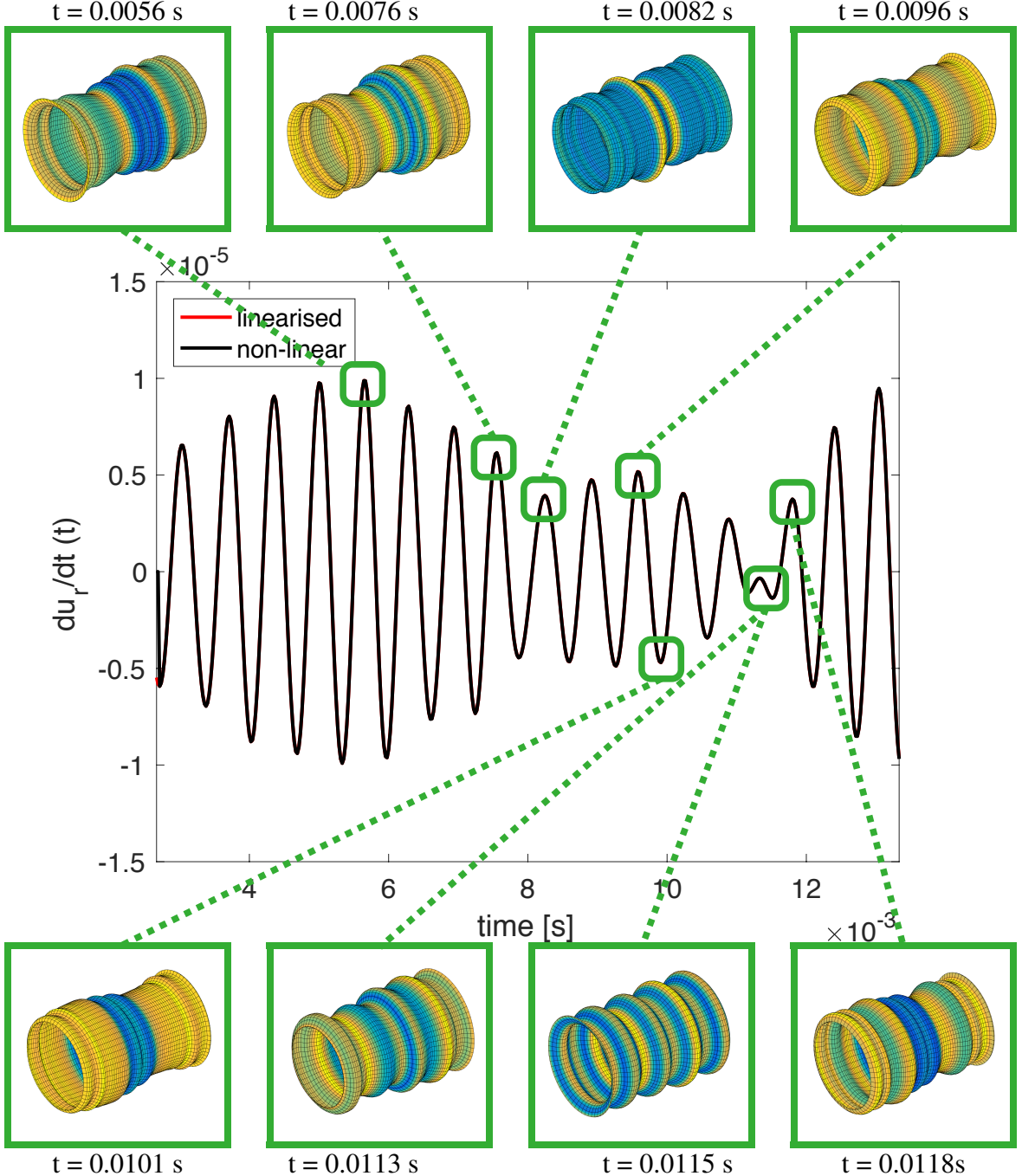


Figure 14: Full magnet problem: Displacements of the OVC at different times for $|J_\phi^{AC}| / |J_\phi^{DC}| = 15\%$ and $\omega = 2\pi(1500)\text{rad/s}$.

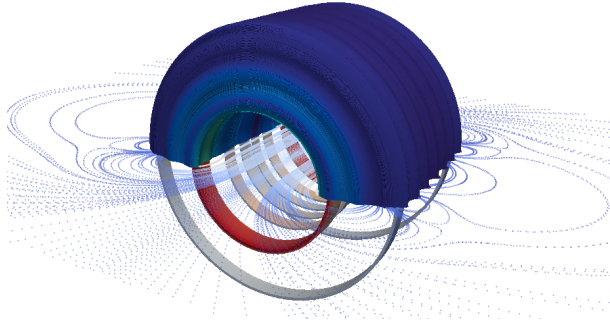


Figure 15: Full magnet problem: Distorted OVC, main coils and corresponding static magnetic field lines for the static problem where $\mathbf{J}^s = \mathbf{J}^{DC}$ and $t = 0\text{s}$.

7 Conclusion

In this paper, we have described a framework for both the *linearised* and *non-linear approaches* to obtain transient solutions to the acousto-magneto-mechanical coupling in MRI scanners. We have provided, through a non-dimensional analysis of the non-linear terms, a set of rigorous bounds which define the non-linearity of the problem in terms of the ratios between the static and gradient current sources and magnetic fields. In terms of the two questions we posed at the start of the paper, through the numerical examples presented in Section 6, we have shown that: 1) there is accurate agreement between the two *approaches* and that, not only does the *linearised approach* provide accurate approximations to the transient response of the fields, but also accurately predicts the quantities of interest and the resonance behaviour of MRI scanners, and 2) the *linearised approach* provides accurate results across the full region of interest in the frequency spectrum $\omega \leq 2\pi[5000]\text{rad/s}$ for a range of current density ratios $J_\phi^{AC}/J_\phi^{DC} \leq 20\%$. In terms of current clinical MRI scanner applications, this ratio is restricted to around 4 – 12% and thus our analysis validates the use of the *linearised approach* in providing accurate solutions in current and future MRI scanner design, with orders of magnitude saving in the computational cost over the *non-linear approach*.

Acknowledgements

The first author gratefully acknowledge the support of EPSRC and Siemens Magnet Technology in the form of a CASE Award PhD Studentship (EP/L505699/1). The second author gratefully acknowledges the financial support received from EPSRC in the form of the grant EP/R002134/1. The third author acknowledges the support received by the Sêr Cymru National Research Network in Advanced Engineering and Materials. The second, third and fourth authors acknowledge the financial support provided by the European Training Network AdMoRe (675919). The non-commercially sensitive data is provided in full in Section 6. The authors are very grateful for the many useful industrial insights provided by Siemens Magnet Technology.

References

- [1] P. Kozlowski, S. D. Chang, E. C. Jones, K. W. Berean, H. Chen, and S. L. Goldenberg, “Combined diffusion-weighted and dynamic contrast-enhanced MRI for prostate cancer diagnosis–correlation with biopsy and histopathology,” *Journal of Magnetic Resonance Imaging*, vol. 24, no. 1, pp. 108–113, 2006.
- [2] A. Brydie and N. Raby, “Early MRI in the management of clinical scaphoid fracture,” *The British Journal of Radiology*, vol. 76, no. 905, pp. 296–300, 2003.
- [3] D. W. Paty, J. J. F. Oger, L. F. Kastrukoff, S. A. Hashimoto, J. P. Hooge, A. A. Eisen, K. A. Eisen, S. J. Purves, M. D. Low, V. Brandejs, W. D. Robertson, and D. K. Li, “MRI in the diagnosis of ms:

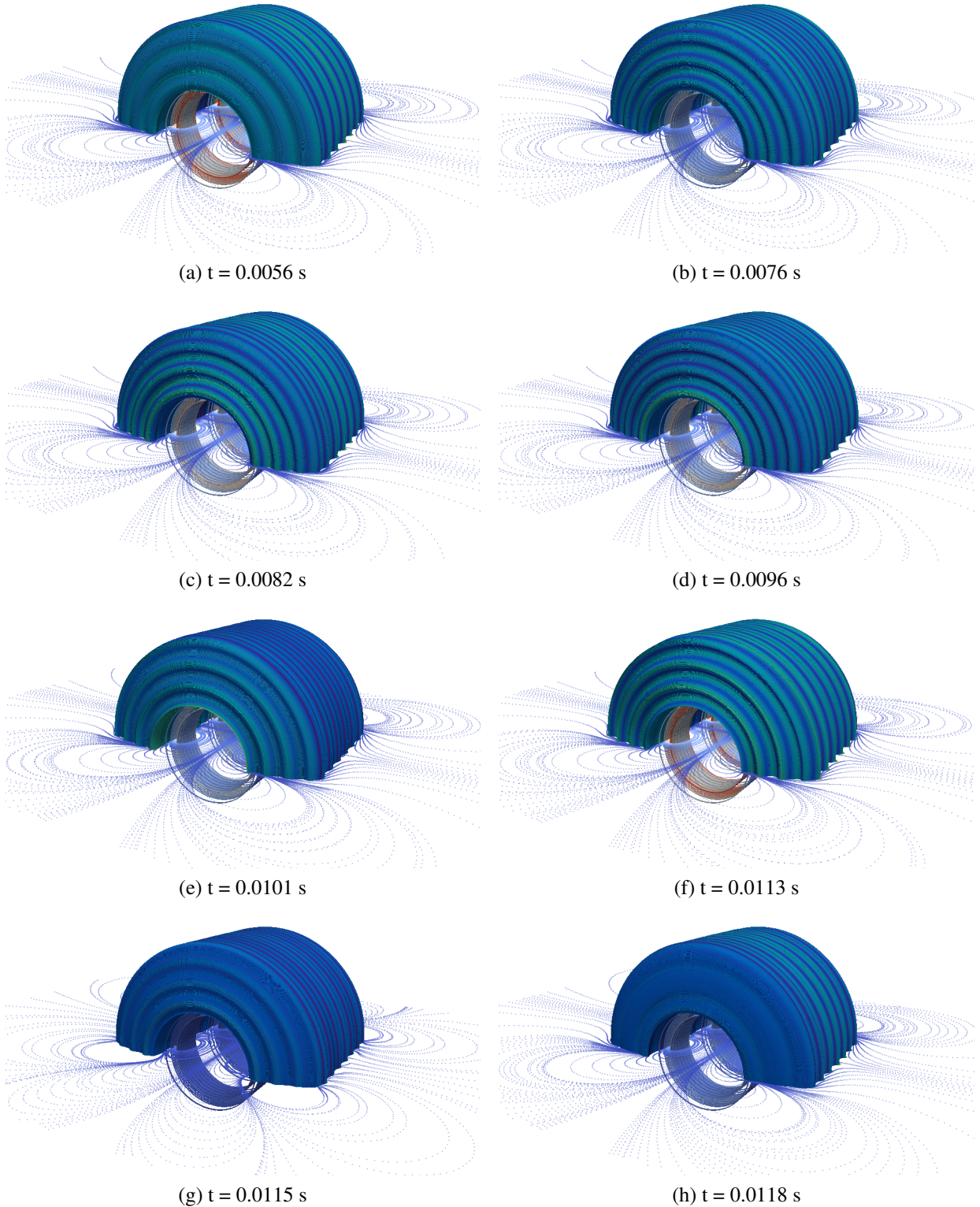


Figure 16: Full magnet problem: Snapshots of the distorted OVC, gradient coils and corresponding gradient magnetic field lines at various time intervals for $|J_\phi^{AC}| / |J_\phi^{DC}| = 15\%$ and $\omega = 2\pi(1500)\text{rad/s}$.

- A prospective study with comparison of clinical evaluation, evoked potentials, oligoclonal banding, and CT,” *Neurology*, vol. 38, no. 2, p. 180, 1988.
- [4] A. P. S. Kirkham, M. Emberton, and C. Allen, “How good is MRI at detecting and characterising cancer within the prostate?,” *European Urology*, vol. 50, no. 6, pp. 1163–1175, 2006.
 - [5] H. U. Ahmed, A. Kirkham, M. Arya, R. Illing, A. Freeman, C. Allen, and M. Emberton, “Is it time to consider a role for MRI before prostate biopsy?,” *Nature Reviews Clinical Oncology*, vol. 6, no. 4, pp. 197–206, 2009.
 - [6] D. Price, I. Delakis, C. Renaud, and R. Dickinson, “MRI scanners: A buyer’s guide.” <https://pdfs.semanticscholar.org/df6b/bd32e99e1889bfcc61001285c6c96297e574.pdf>. Accessed: 25/06/2017.
 - [7] Siemens, “MAGNETOM family of MRI systems.” <http://www.deltamedicalsystems.com/DeltaMedicalSystems/media/Product-Details/MAGNETOM-Family-Brochure.pdf>. Accessed 25/06/2017.
 - [8] Siemens, “Magnetic resonance imaging: The definitive portfolio for MRI.” <https://www.healthcare.siemens.com/magnetic-resonance-imaging?stc=wwhim800053>. Accessed 25/06/2017.
 - [9] A. G. van der Kolk, J. Hendrikse, J. J. M. Zwanenburg, F. Visser, and P. R. Luijten, “Clinical applications of 7T MRI in the brain,” *European Journal of Radiology*, vol. 82, no. 5, pp. 708–718, 2013.
 - [10] G. A. Kerchner, “Ultra-high field 7T MRI: A new tool for studying alzheimer’s disease,” *Journal of Alzheimer’s Disease*, vol. 26, no. 3, pp. 91–95, 2011.
 - [11] Siemens, “Magnetom terra: Translate 7t research power into clinical care.” <https://www.healthcare.siemens.co.uk/magnetic-resonance-imaging/7t-mri-scanner/magnetom-terra>. Accessed: 17/11/2017.
 - [12] N. Savage, “The world’s most powerful MRI takes shape.” <http://spectrum.ieee.org/biomedical/imaging/the-worlds-most-powerful-mri-takes-shape>. Accessed: 30/06/2017.
 - [13] S. Bagwell, P. D. Ledger, A. J. Gil, M. Mallett, and M. Kruip, “A linearised hp -finite element framework for acousto-magneto-mechanical coupling in axisymmetric MRI scanners,” *International Journal for Numerical Methods in Engineering*, 2017. DOI: 10.1002/nme.5559.
 - [14] T. C. Cosmus and M. Parizh, “Advances in whole-body MRI magnets,” *IEEE Transactions on Applied Superconductivity*, vol. 21, no. 3, pp. 2104–2109, 2011.
 - [15] G. Giovannetti, V. Hartwig, V. Viti, P. Zadaricchio, L. Meini, L. Landini, and A. Benassi, “Low field elliptical MR coil array designed by FDTD,” *Concepts in Magnetic Resonance Part B: Magnetic Resonance Engineering*, vol. 33B, no. 1, pp. 32–38, 2008.
 - [16] A. Trakic, H. Wang, F. Liu, H. S. Lopez, and S. Crozier, “Analysis of transient eddy currents in MRI using a cylindrical FDTD method,” *IEEE Transactions on Applied Superconductivity*, vol. 16, no. 3, pp. 1924–1936, 2006.
 - [17] F. Liu and S. Crozier, “An FDTD model for calculation of gradient-induced eddy currents in MRI system,” *IEEE Transactions on Applied Superconductivity*, vol. 14, no. 3, pp. 1983–1989, 2004.
 - [18] H. Zhao, S. Crozier, and F. Liu, “Finite difference time domain (FDTD) method for modeling the effect of switched gradients on the human body in MRI,” *Magnetic Resonance in Medicine*, vol. 48, no. 6, pp. 1037–1042, 2002.
 - [19] F. Liu, S. Crozier, H. Zhao, and B. Lawrence, “Finite-difference time-domain-based studies of MRI pulsed field gradient-induced eddy currents inside the human body,” *Concepts in Magnetic Resonance*, vol. 15, no. 1, pp. 26–36, 2002.
 - [20] F. Liu, H. Zhao, and S. Crozier, “Calculation of electric fields induced by body and head motion in high-field MRI,” *Journal of Magnetic Resonance*, vol. 161, no. 1, pp. 99–107, 2003.
 - [21] M. Kozlov and R. Turner, “Fast MRI coil analysis based on 3-D electromagnetic and RF circuit co-simulation,” *Journal of Magnetic Resonance*, vol. 200, no. 1, pp. 147–152, 2009.
 - [22] J. M. B. Kroot, “Analysis of eddy currents in a gradient coil,” *Scientific Computing in Electrical Engineering*, vol. 9, pp. 221–226, 2006.

- [23] D. W. Markiewicz, M. R. Vaghar, I. R. Dixon, and H. Garmestani, “Generalized plane strain analysis of superconducting solenoids,” *Journal of Applied Physics*, vol. 86, no. 12, pp. 7039–7051, 1999.
- [24] L. Li, J. Cheng, C. Cui, Y. Li, Y. Dai, X. Hu, J. Liu, L. Wang, and Q. Wang, “Numerical analysis of mechanical behavior for a 9.4-T whole-body MRI magnet,” *IEEE Transactions on Applied Superconductivity*, vol. 27, no. 4, pp. 1–5, 2017.
- [25] J. Chen and X. Jiang, “Stress analysis of a 7 T actively shielded superconducting magnet for animal MRI,” *IEEE Transactions on Applied Superconductivity*, vol. 22, no. 3, pp. 4903104–4903104, 2012.
- [26] Y. Dai, Q. Wang, C. Wang, L. Li, H. Wang, Z. Ni, S. Song, S. Chen, B. Zhao, H. Wang, Y. Li, X. Hu, C. Cui, J. Cheng, Y. Lei, and L. Yan, “Structural design of a 9.4 T whole-body MRI superconducting magnet,” *IEEE Transactions on Applied Superconductivity*, vol. 22, no. 3, pp. 4900404–4900404, 2012.
- [27] W. Shao and C. K. Mechefske, “Acoustic analysis of a gradient coil winding in an MRI scanner,” *Concepts in Magnetic Resonance Part B: Magnetic Resonance Engineering*, vol. 24B, no. 1, pp. 15–27, 2005.
- [28] Y. Wang, F. Liu, and S. Crozier, “Simulation study of noise reduction methods for a split MRI system using a finite element method,” *Medical Physics*, vol. 42, no. 12, pp. 7122–7131, 2015.
- [29] Y. Wang, F. Liu, E. Weber, F. Tang, J. Jin, Y. Tesiram, and S. Crozier, “Acoustic analysis for a split MRI system using FE method,” *Concepts in Magnetic Resonance Part B: Magnetic Resonance Engineering*, vol. 45, no. 2, pp. 85–96, 2015.
- [30] J. C. Lin and Z. Wang, “Acoustic pressure waves induced in human heads by RF pulses from high-field MRI scanners,” *Health Physics*, vol. 98, pp. 603–613, 2010.
- [31] M. Guan, X. Wang, L. Ma, Y. Zhou, and C. Xin, “Magneto-mechanical coupling analysis of a superconducting solenoid magnet in self-magnetic field,” *IEEE Transactions on Applied Superconductivity*, vol. 24, no. 3, pp. 1–4, 2014.
- [32] M. Rausch, M. Gebhardt, M. Kaltenbacher, and H. Landes, “Magnetomechanical field computations of a clinical magnetic resonance imaging (MRI) scanner,” *The International Journal for Computation and Mathematics in Electrical and Electronic Engineering (COMPEL)*, vol. 22, pp. 576–588, 2003.
- [33] M. Rausch, M. Gebhardt, M. Kaltenbacher, and H. Landes, “Computer-aided design of clinical magnetic resonance imaging scanners by coupled magnetomechanical-acoustic modeling,” *IEEE Transactions on Magnetics*, vol. 41, pp. 72–81, 2005.
- [34] P. D. Ledger, A. J. Gil, R. Poya, M. Kruip, I. Wilkinson, and S. Bagwell, “Solution of an industrially relevant coupled magneto-mechanical problem set on an axisymmetric domain,” *Applied Mathematical Modelling*, vol. 40, pp. 1959–1971, 2016.
- [35] L. Demkowicz, *Computing with hp-adaptive Finite Elements: Volume 1 One and Two Dimensional Elliptic and Maxwell Problems*. Chapman and Hall/CRC, 2006.
- [36] B. Szabó and I. M. Babuška, *Finite Element Analysis*. John Wiley and Sons, 1991.
- [37] H. A. Wheeler, “Formulas for the skin effect,” *Proceedings of the IRE*, vol. 30, no. 9, pp. 412–424, 1942.
- [38] A. J. Gil and J. Bonet, “Finite element analysis of prestressed structural membranes,” *Finite Elements in Analysis and Design*, vol. 42, no. 8-9, pp. 683–697, 2006.
- [39] A. J. Gil, “Structural analysis of prestressed saint venant-kirchhoff hyperelastic membranes subjected to moderate strains,” *Computers and Structures*, vol. 84, no. 15-16, pp. 1012–1028, 2006.
- [40] A. J. Gil and J. Bonet, “Finite element analysis of partly wrinkled reinforced prestressed membranes,” *Computational Mechanics*, vol. 40, no. 3, pp. 595–615, 2007.
- [41] R. Poya, R. Sevilla, and A. J. Gil, “A unified approach for a posteriori high-order curved mesh generation using solid mechanics,” *Computational Mechanics*, 2016.
- [42] S. Baek, R. L. Gleason, K. R. Rajagopal, and J. D. Humphrey, “Theory of small on large: Potential utility in computations of fluid-solid interactions in arteries,” *Computer Methods in Applied Mechanics and Engineering*, vol. 196, pp. 3070–3078, 2007.
- [43] P. Sprawls, *Magnetic Resonance Imaging: Principles, Methods, and Techniques*. Medical Physics Publishing, 2000.
- [44] J. Bonet and R. D. Wood, *Nonlinear Continuum Mechanics for Finite Element Analysis*. Cambridge

University Press, 1997.

- [45] P. Monk, *Finite Element Methods for Maxwell's Equations*. Oxford University Press, 2003.
- [46] T. Kupiszewski and O. R. Christianson, “Conceptual design of superconducting magnet coils.” <http://aries.ucsd.edu/LIB/REPORT/SPPS/FINAL/chap4.pdf>, 1997.
- [47] D. J. Griffiths, *Introduction to Electrodynamics*. Pearson Education, 2014.
- [48] P. Bettess, *Infinite Elements*. Penshaw Press, 1992.
- [49] T. Liu, C. Zhao, Q. Li, and L. Zhang, “An efficient backward euler time-integration method for nonlinear dynamic analysis of structures,” *Computers & Structures*, vol. 106, pp. 20–28, 2012.
- [50] P. J. Roache and D. E. Dietrich, “Evaluation of the filtered leapfrog-trapezoidal time integration method,” *Numerical Heat Transfer*, vol. 14, no. 2, pp. 149–164, 1988.
- [51] W. A. Artuzi, “Improving the newmark time integration scheme in finite element time domain methods,” *IEEE Microwave and Wireless Components Letters*, vol. 15, no. 12, pp. 898–900, 2005.
- [52] J. Chung and G. M. Hulbert, “A time integration algorithm for structural dynamics with improved numerical dissipation: The generalized- α method,” *Journal of Applied Mechanics*, vol. 60, pp. 371–375, 1993.
- [53] R. K. Brayton, F. G. Gustavson, and G. D. Hachtel, “A new efficient algorithm for solving differential-algebraic systems using implicit backward differentiation formulas,” *Proceedings of the IEEE*, vol. 60, no. 1, pp. 98–108, 1972.
- [54] A. H. van Zuijlen and H. Bijl, “Implicit and explicit higher order time integration schemes for structural dynamics and fluid-structure interaction computations,” *Computers & Structures*, vol. 83, no. 2, pp. 93–105, 2005.
- [55] H. Spachmann, R. Schuhmann, and T. Weiland, “Higher order explicit time integration schemes for Maxwell’s equations,” *International Journal of Numerical Modelling: Electronic Networks, Devices and Fields*, vol. 15, no. 5–6, pp. 419–437, 2002.
- [56] A. N. Brooks and T. J. R. Hughes, “Streamline upwind/Petrov-Galerkin formulations for convection dominated flows with particular emphasis on the incompressible Navier-Stokes equations,” *Computer Methods in Applied Mechanics and Engineering*, vol. 32, no. 1–3, pp. 199–259, 1982.
- [57] K. E. Jansen, C. H. Whiting, and G. M. Hulbert, “A generalized- α method for integrating the filtered Navier-Stokes equations with a stabilized finite element method,” *Computer Methods in Applied Mechanics and Engineering*, vol. 190, no. 3, pp. 305–319, 2000.
- [58] D. Engwirda, “MESH2D – Delaunay-based unstructured mesh-generation.” <https://uk.mathworks.com/matlabcentral/fileexchange/25555-mesh2d-delaunay-based-unstructured-mesh-generation>. Accessed 18/09/2017.
- [59] S. Bagwell, *A Numerical Multi-Physics Approach to Understanding MRI Scanners and their Complex Behaviour*. PhD thesis, Swansea University, UK. *In Preparation*. 2018.